Feasibility study of reactive mass transport modelling to support service life design

Numerical simulation of chloride ingress

Marcos Meson, Victor; Michel, Alexander; Geiker, M.R.

Link to article, DOI:
10.11581/dtu.00000236

Publication date:
2022

Document Version
Publisher's PDF, also known as Version of record

Feasibility study of reactive mass transport modelling to support service life design

Numerical simulation of chloride ingress

V. Marcos Meson

A. Michel

M.R. Geiker

May 2022

Feasibility study of reactive mass transport modelling to support service life design
Numerical simulation of chloride ingress

Report
2022

By
V. Marcos Meson
A. Michel
M.R. Geiker

Cover photo: [Tekst]
Published by: DTU, Department of Civil Engineering, Brovej, Building 118, 2800 Kgs. Lyngby Denmark
www.byg.dtu.dk
ISSN: [0000-0000] (electronic version)
ISBN: [000-00-0000-000-0] (electronic version)

ISSN: [0000-0000] (printed version)
ISBN: [000-00-0000-000-0] (printed version)

Feasibility study of reactive mass transport modelling to support service life design

– *Numerical simulation of chloride ingress*

This report summarizes the results of a numerical study of chloride ingress and reinforcement corrosion initiation using a reactive mass transport (RMT) model. The study explores the applicability of a RMT model developed at DTU for civil engineering projects.

1th February 2022

Victor Marcos Meson

vmmn@cowi.com

Alexander Michel

almic@byg.dtu.dk

Department of Civil Engineering, Technical University of Denmark

Copenhagen, Denmark

Mette Rica Geiker

mette.geiker@ntnu.no

Department of Structural Engineering, Norwegian University of Science and Technology

Trondheim, Norway

PREFACE

This study comprises a feasibility study of reactive mass transport modelling to support the service life design of reinforced concrete structures exposed to chlorides.

The study was undertaken as part of the collaboration project *"Fergefri E39, forskning knyttet til Gjennomføring, utførelse, analyse og dimensjonering av store og avanserte betongkonstruksjoner i utsatt miljø"*, between Statens vegvesen and NTNU.

The work has been carried out by researcher/postdoc Victor Marcos Meson (DTU) in collaboration with Professor Mette Geiker (NTNU) and Professor Alexander Michel (DTU).

ACKNOWLEDGEMENTS

The main author would like to acknowledge the contribution of Alexander Michel and Mette Geiker on the outline and preparation of this investigation and report. Also, the contribution of Marvin Glissner with his work from his MSc thesis: *"Service life prediction of concrete in cold climate, benchmarking of chloride ingress"*, and Sharmilan Suntharalingam with his modelling advice.

ABSTRACT

This report discussed the applicability of reactive mass transport (RMT) models for the durability design of concrete structures. The study focussed on supporting service life modeling of chloride-induced reinforcement corrosion of immersed concrete structures in the Norwegian coastline.

First, model results were compared to experimental data of selected case studies for chloride ingress in mortar and concrete mixes. The modeled data showed a relatively good agreement with the experimental results of concrete specimens exposed to seawater in the Norwegian Atlantic coast for 25 years.

Second, a parametric study was carried out to evaluate the model performance to predict the minimum concrete cover required to avoid chloride-induced corrosion of reinforcing steel in a concrete element immersed in seawater. A sensitivity study covering the main model input parameters was carried out using the Partial Least-Square (PLS) method. The results of the study indicated that model uncertainty does not solely comprise parameters that must be adjusted (e.g., the tortuosity factor) but also parameters that shall be selected based on engineering judgment.

Third, a machine-learning-based regression model was trained using the parametric study results to provide a fast interpolation method between the parameter study variables. The regression model effectively provided fast and consistent interpolation between the data.

The methodology presented in this study has shown an excellent potential to be implemented in existing performance-based durability models, such as *fib* Model Code 34, where RMT models can provide a robust physically-based transport model to replace existing analytical solutions.

TABLE OF CONTENTS

1. INTRODUCTION

1.1 Background

Design and maintenance of concrete civil infrastructure, often with service life expectancy over 100 years, leads to challenges when predicting the concurring deterioration processes and outlining design solutions. Prevention of corrosion of the steel reinforcement is one of the critical aspects to be addressed. The design is either based on deem-to-satisfy approaches from international standards [1] (and corresponding national annexes) or performance-based design methods [2]. Currently, the European standards provide recommendations for a design service life up to 100 years [3]. However, current trends are to design concrete infrastructure for even longer service life. Performance-based models could potentially be used for such service-life predictions [4], yet there is criticism regarding the applicability of the current approaches [5–8]. Notably, models based on the error function approximation to Fick's diffusion law (e.g. applied in DuraCrete [9] and the *fib* Model Code for Service Life Design [2]) are susceptible to parameters such as the "ageing exponent " [10], the "critical chloride content" [8], and the " chloride content at the surface" [5,11]. These parameters are generally derived from experimental data and cannot be generalized to any binder system or exposure conditions [12].

Ongoing development within the cement and concrete industry, e.g. new binder compositions containing, for example, calcined clays or bio-fly-ash, more advanced mix-designs, or alternative reinforcement systems (e.g. fibre reinforcement), challenges the application of the current design tools. Reactive mass transport (RMT) models represent a more physicochemically sound and generally applicable alternative. RMT models describe the interaction between solids, ions, liquids, and gasses, which allow for a more detailed understanding of chloride ingress and other species. Examples of numerous applications in the geochemical field [13] and the concrete-technology field [14–16] show the enormous potential of these models. However, further work is needed to help understand and address the added complexity of the models and their impact on the uncertainty of the predictions [17].

This investigation covers the application of a RMT model for the simulation of chloride ingress and the prediction of initiation of corrosion of reinforced concrete exposed to seawater in Norway. The applied RMT model is based on the work presented in [18,19] and still under development.

1.2 Aim and Objectives

The work aimed to undertake numerical simulation of chloride ingress in marine exposed concrete through reactive mass transport (RMT) modelling to potentially support service life design of concrete structures for the E39 Coastal Highway Route project. The following objectives were identified:

1. Compare the predictive capability of the existing RMT model with laboratory and field data.
2. Quantify the sensitivity of the RMT model output concerning main model parameters.
3. Illustrate and discuss the applicability of RMT models for engineering problems within the context of concrete infrastructure service life design.

1.3 Scope and limitations

The scope of this work was to study the applicability of RMT models for their use as a tool for the durability design of concrete structures and outline possible implementation strategies. The following limitations apply:

1. The results and discussion are to be considered research-focused and not intended for direct engineering applications.
2. The model predictions presented are illustrative and not intended to provide an accurate calculation of service-life design parameters.

3. The study only covers the application of the selected RMT model to predict the chloride and pH in the pore solution of uncracked concrete fully immersed in seawater. Other exposure conditions are not covered.
4. The limit state considered for the service-life verification is the de-passivation of carbon-steel embedded in concrete induced by chlorides assuming different limit state parameters (total chloride concentration, free chloride concentration, and $[Cl^-]/[OH^-]$ ratio). The propagation of corrosion or other deterioration phenomena are not covered. Data regarding threshold values for corrosion initiation were selected based on the work in [20]. Reference limit values for typical engineering applications are considered from [2]. The threshold values leading to initiation of reinforcement corrosion considered in this study are shown in Table 1.

Table 1 Threshold values considered for initiation of chloride-induced reinforcement corrosion, total chlorine content (Cl_{elem}), chloride ion concentration in the pore solution ($[Cl^-]/[OH^-]$, and chloride-to-hydroxyl ion concentration in the pore solution

Parameter	Ref	Range	Characteristic Value (assumed)	Units
$Cl_{elem.}$	[2,20]	0.04 – 8.34	0.5	%-wt_{bw}
$[Cl^-]$	[20]	0.045 – 3.22	0.2	mol/kg_w
pH	[21]	8-11	9	-
$[Cl^-]/[OH^-]$	[20]	0.09 – 45	0.5	-

1.4 Background information and data

Experimental data from former investigations support this investigation, the following data was used:

1. Material data regarding binder compositions were taken from [22–25], and mix-design proportions were taken from [24,26–28].
2. Boundary conditions were considered based on the data in [24,26,27] and [28], supported by Norwegian climate and seawater chemistry data in [23,29]
3. Experimental data from [24,26,27] was used for validation with exposure in laboratory conditions; and data from [28] (supported with data from [30]) for the exposure in field conditions.
4. Binder compositions considered in the parameter study among others include fly ash and silica fume which were used in a parallel experimental study on mix design of concrete with a target compressive strength of 100 MPa at 91 days [31,32], however only up to maximum 30 % fly ash and 10 % silica fume.

The numerical results produced in this study can be accessed in [33].

2. NUMERICAL SIMULATION OF CHLORIDE INGRESS

This section describes the applied model and outlines the main input parameters considered for the modelling approach used in this report.

2.1 Applied model

The modelling framework (i.e., the RMT model), sketched in Figure 1, comprises three groups of models sequentially running in closed-loop iterations (after [19]) in the following order:

1. **Mass transport.** An ionic transport problem solved numerically using FEM and applying the extended Poisson–Nernst–Planck (PNP) equations (presented in [14]).
2. **Chemical reactions.** A thermodynamic model solved in Phreeqc [34] using the thermodynamic data in [35]. Physical adsorption of chloride in the C-S-H is calculated separately based on a Langmuir expression solved discretely before using the thermodynamic solver (see [36]).
3. **Pore structure.** A microstructure model based on the bundle-of-tubes model described and tested in [19].

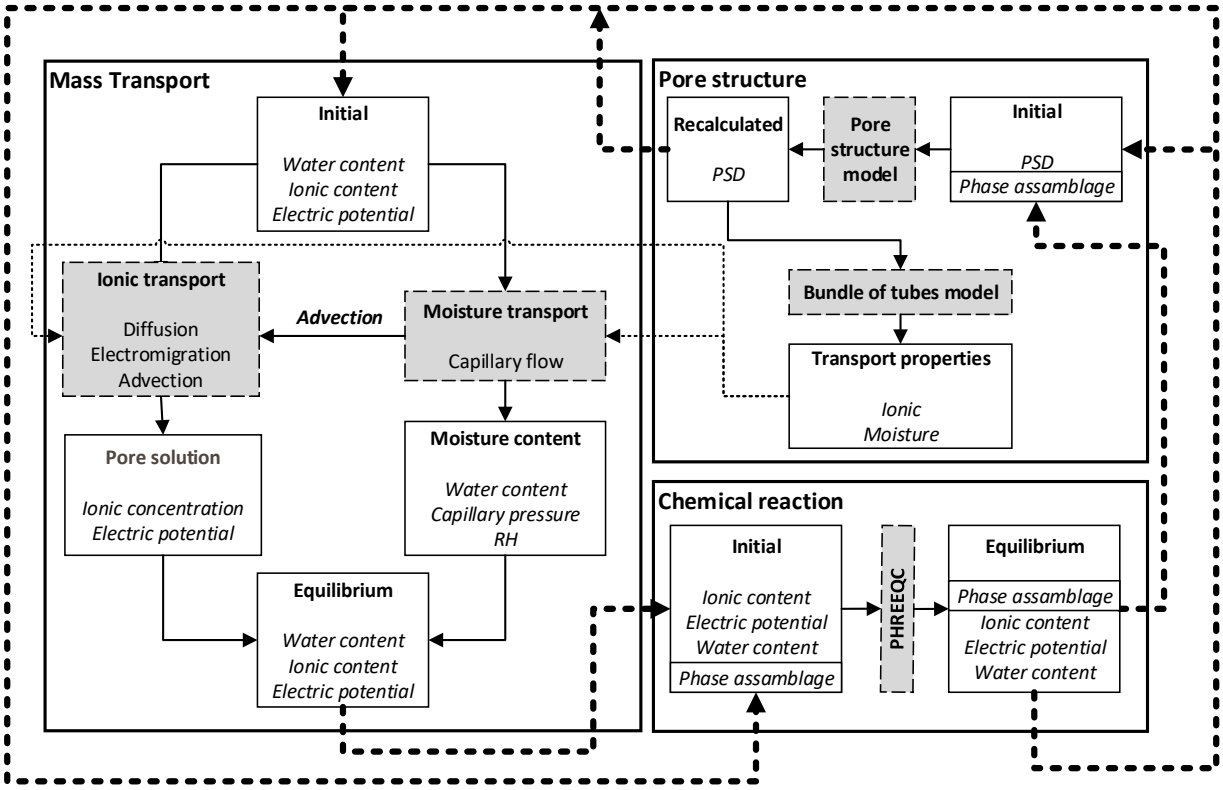

Figure 1 The applied modelling framework, after [19].

The modelling framework is based on [14] and further developed in [19]. The model capabilities and the main group of model input parameters in this report is described below.

1. **The mass transport model:** calculates the concentration of ions in the pore solution as they move through the pore structure, additional transport of moisture and gas may be simulated. The main input parameters are:
    a. The space (length) of the modelled domain and the element mesh size
    b. The exposure time and the time-step size

c. The tortuosity factor describing the impact of the overall pore structure (and other factors not explicitly accounted for) on the overall rate of transport. Note that the tortuosity factor was fitted when testing the model against experimental data.
   The term “tortuosity factor” refers herein to the effect of tortuosity in the transport of dissolved ionic species. In this model, the tortuosity factor represents the inverse of the pore structure tortuosity (i.e. as tortuosity increases, the tortuosity factor decreases and transport of dissolved secies).
d. The exposure (boundary) conditions including the concentration of dissolved ionic species, the electric potential (when relevant), temperature, and pressure
e. The pre-selected ionic species present in the system
f. The physics included in the model (some de-selected depending on the specific case).
   i. Fickian diffusion of dissolved ionic species and gas in partially saturated media
   ii. Electromigration of dissolved ionic species
   iii. Moisture transport through capillary pressure (e.g. Richard's equation)
   iv. Advective transport of dissolved ionic species

2. **The chemical reaction model (i.e. Phreeqc):** recalculates the ionic concentration in the pore solution and the composition of the solid phases based on the chemical equilibrium equations specified in the chemical database (i.e. Cemdata). The main input parameters are:
   a. The binder system described by the content and degree of reaction of the oxides composing the binder
   b. The concrete mix-design including the cement composition and content, water-to-cement ratio, and entrained and entrapped air content
   c. The pre-selected chemical species used in the chemical speciation model (PHREEQC) and the chemical database used (Cemdata)
3. **Pore structure:** the pore structure described by the pore-size distribution (PSD) of the hardened cement paste. The main input parameters and methods of calculation are
   a. The initial PSD estimated based on experimental data
   b. The relation between the changes in volume fraction of solids and the PSD is based on a study presented in [23], i.e., changes in the PSD are continuously recalculated as the content and proportion of solid phases change. In addition, changes in the transport properties of the cement paste are recalculated from changes in the PSD.
   c. The relation between the PSD and the transport parameters is based on semi-empirical relations derived using the bundle-of-tubes model (e.g. physical phenomena calibrated to experiments), see e.g., [23].

2.2 Main equations and main input parameters for models

2.2.1 Transport of ionic species

The mass-transport model employed in the present investigations is a simplification of the model presented in [18,19]. The numerical model solves an extended version of the Poisson-Nernst-Planck (PNP) equation system, derived in [14]. The model is discretized for a partially saturated system with a negligible impact of the electromigration and convection term (i.e. diffusion is the governing transport mechanism). The governing mass transport equation is then written as follows:

$$\varepsilon \frac{\partial c_i}{\partial t} + c_i \frac{\partial \varepsilon}{\partial t} = \nabla(D_i \varepsilon \nabla c_i + D_i c_i \nabla \varepsilon) + q_i \qquad \text{Eq. 1}$$

where D_i is the effective diffusion coefficient of the i^{th} species in the liquid phase and q_i the mass exchange term for chemical interactions between the i^{th} species.

A finite element approach is used to solve the mass transport problem see, *e.g.* [37]. The weak-form of the governing equations is obtained using the Green-Gauss theorem, applying a one-dimensional Galerkin's discretization to the spatial domain with linear elements. Time discretization is carried out using a single parameter implicit time integration scheme with a modified Newton-Raphson scheme, as described in [18,19].

The transport of dissolved ions through the pore structure is described using a bundle of tubes model, based on the implementation of [38] in [19]. The model describes changes of the pore-size distribution and corresponding ionic transport properties due to dissolution and formation of phases, calculated by the chemical equilibrium model [39].

The relation between the ionic transport in cement paste and bulk water is made by a tortuosity factor, T_k, which ranges between zero and one and accounts for effects on the ideal diffusion coefficient of each ion in water, D^i, as follows:

$$D_{eff}^{i} = D^{i}(\frac{1}{T_k}) \quad \text{Eq. 2}$$

where D_{eff}^{i} is the effective diffusion coefficient of the ith ionic species and T_k the tortuosity factor for time-step "k" . T_k is recalculated after each determination of the chemical equilibrium to account for the impact on the pore structure of changes in the phase assemblage, following a sigmoid function:

$$T_k = T_{min} + (1 - T_{min})\, P_k^{\left(\frac{\log\left(\frac{T_0 - T_{min}}{1 - T_{min}}\right)}{\log(P0)}\right)} \quad \text{Eq. 3}$$

where T_{min} is a lower limit assigned to the tortuosity factor when the pore volume reaches a near-zero value, T_0 is a reference tortuosity factor assumed at the beginning of the exposure, P_0 is the total pore volume at the beginning of the exposure and P_k is the total pore volume at the time-step "k". So that, $P_k = 1 \rightarrow T_k = 1 \rightarrow D_{eff}^{i} \equiv D^{i}$, and $P_k = 0 \rightarrow T_k = \text{inf} \rightarrow D_{eff}^{i} \approx 0$.

2.2.2 Thermodynamic equilibrium

Chemical equilibrium is solved through a coupled thermodynamic solver, i.e., the geochemical code IPHREEQC [40] and the thermodynamic database Cemdata 18 [35]. The thermodynamic solver calculates the reactions among ionic species in the liquid phase and the equilibrium between the ionic constituents in the liquid phase and the solid phases. In the present study, gaseous species are only considered ideally dissolved in solution, and liquid-gas phase interactions are neglected.

The phase assemblages considered are based on data from [26] for the laboratory exposure case study and data from [41,42] for the field exposure and parameter study.

2.2.3 Development of hydration

The degree of hydration (α) of the main oxides during the exposure is calculated based on the hydration model from [43], implemented in the RMT model framework in [19], see Eq. 4.

$$\frac{d\alpha}{dt} = \left[\exp\left(\frac{E_t}{R}\left(\frac{1}{T_r} - \frac{1}{T}\right)\right)\right] \cdot \left[\left(\alpha_u \frac{\beta}{M}\left(\frac{S}{M}\right)^{\beta}\right)\exp\left(-\left(\frac{S}{M}\right)^{\beta}\right)\right] \quad \text{Eq. 4}$$

$$\frac{dM}{dt} = \left[\exp\left(\frac{E_t}{R}\left(\frac{1}{T_r} - \frac{1}{T}\right)\right)\right] \quad \text{Eq. 5}$$

The first term on the right-side of Eq. 4 corresponds to the Arrhenius equation where E_t is the activation energy, R the universal gas constant, T the temperature, and T_{ref} the reference temperature. The second term on the right-side represents the hydration law where M is the equivalent maturity of the binder (i.e. each oxide in the model) according to Eq. 5, T_r a reference temperature, and T the exposure temperature. The model parameters used in the present study for the hydration model are summarized in Table 2.

Table 2 Assumed input parameters for the hydration model in this study (same for all binders).

Parameter	Units	Value
Et	J/mol	25000
R	J/(mol K)	8.31446
β	-	0.35
S	-	30
α_u	%	See Table 5

2.2.4 Physical binding of chloride

The physical binding of dissolved chloride ions (i.e. Cl^-), adsorbed onto the C-S-H surface (θ_A) is modelled by a Langmuir isotherm, based on the work by Glissner [36]:

$$\theta_A = \frac{V}{V_m} = \frac{K_{eq}^A \cdot C_A}{1 + K_{eq}^B \cdot C_A} \quad \text{Eq. 6}$$

where V/V_m is the ratio of free-to-bound chloride per unit mass of C-S-H, $K_{eq}^A \equiv K_{eq}^B$ represent the binding coefficient, and C_A the concentration of free chloride in the solution. Finally, the ratio V/V_m was adjusted to factor γ, so that $\theta_A = V/V_m * \gamma$ and $0 < \gamma < 1$; in order to limit the total binding capacity of the C-S-H. The input data used to estimate the binding model parameters were obtained from the analysis in [36] of the data presented in [24,26]. The binding isotherms derived in [36] are shown in Figure 2 alongside the binding isotherm assumed for the calculations in this report. The binding parameter estimated in [36] and the values selected for the calculations in this report are shown in Table 3

Note that the amount of physical binding was varied when testing the model against experimental data.

Table 3 Adjusted Langmuir Isotherm parameters from [36] and values assumed for this study.

Parameter	NaCl exposure			CaCl exposure			Selected values
	P	M	ML	P	M	ML	
$\log(K_{eq}^A)$	-8.11	-6.44	-6.17	-6.57	-4.61	-4.34	-6.4
$\log(K_{eq}^B)$	-8.11	-6.44	-6.17	-6.57	-4.89	-4.42	-6.4
γ	Not calculated			Not calculated			0. 3 – (0.6) *[1]

*[1] *Values range tested against experimental data. Value shown in brackets was used in the subsequent studies.*

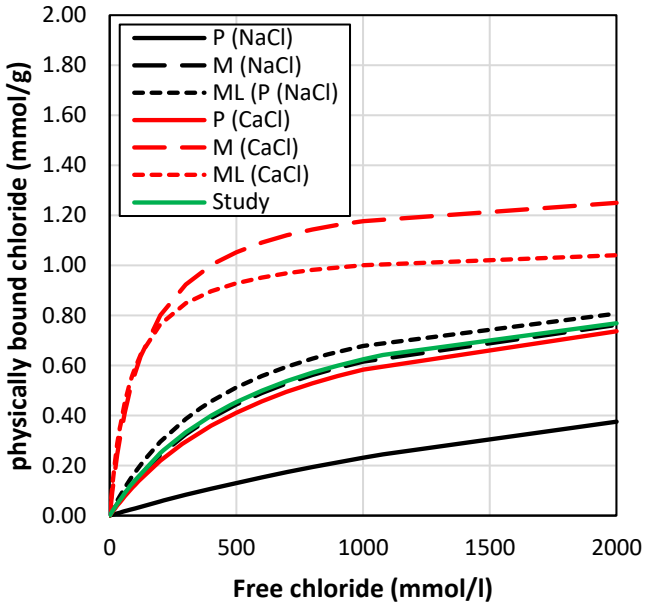

Figure 2 Langmuir isotherms for physical chloride binding by C-S-H calculated in [36], fitted experimental data from [24,26]. The isotherm selected for this study is shown in green.

3. INPUT DATA

This section describes the input parameters used for both the case studies and the parameter study, except that input parameters used to describe development of hydration (Section 2.3.3) and physical binding of chloride (Section 2.2.4)

3.1 Binder compositions and maximum degree of hydration

The main oxides composing the binders considered for the case studies and the parametric study are presented in Table 4 based on the data presented in [22–25]. The oxide compositions of the binder blends considered in the case studies and in the parametric study are given in Table 7 and Table 17, respectively.

The maximum degree of hydration for each oxide (i.e. at an infinite time) used as input in the hydration model in this study is based on an estimate of expected values reported in various references; see references in Table 5.

Table 4 Assumed oxide composition of binders used in this study (units in %-wt).

Oxide	**Portland (PC)**	**White Portland (wPC)**	**Fly ash (FA)**	**Silica fume (SF)**	**Metakaolin (MK)**	**Limestone (LL)**
Ref	[22]	[24]	[22]	[23]	[24]	[24], [25]
CaO	61.71	66.10	4.89	0.10	0.22	53.73
SiO_2	20.40	21.80	56.80	95.10	52.84	3.92
Al_2O_3	4.77	3.56	24.30	1.00	39.49	0.33
Fe_2O_3	3.43	0.24	6.90	0.10	1.42	0.14
SO_3	3.48	0.43	0.64	0.00	0.06	0.05
K_2O	0.92	0.04	1.68	1.00	1.00	0.05
Na_2O	1.08	1.10	1.68	0.10	0.05	0.08
MgO	2.19	3.37	1.74	0.40	0.48	0.35
Cl *[1]	0.07	0.003	0.00	0.00	0.00	0.000
CO_2 *[2]	1.14	2.00	0.00	0.00	3.55*[3]	40.07
TOTAL	99.18	98.64	98.63	97.80	99.11	98.72

*[1] Cl content is calculated as NaCl equivalent.

*[2] CO_2 values are adjusted based on the expected phase assemblage of modern binders (see calculations in appendix A) and LOI values given in the reference publications.

Table 5 Assumed maximum degree of hydration (α_u) of the main oxides for the binders used in this study.

Oxide	Portland (PC)	White Portland (wPC)	Fly ash (FA)	Silica fume (SF)	Metakaolin (MK)	Limestone (LL)
Refs	[25]	[27]	[44–46]	[47]	[27]	[25] *1
CaO	0.85	0.85	0.50	0.85	0.50	0.50
SiO_2	0.85	0.85	0.50	0.85	0.50	0.50
Al_2O_3	0.85	0.85	0.50	0.85	0.50	0.50
Fe_2O_3	0.50	0.50	0.50	0.50	0.50	0.50
SO_3	0.85	0.85	0.50	0.85	0.50	0.50
K_2O	0.85	0.85	0.50	0.85	0.50	0.50
Na_2O	0.85	0.85	0.50	0.85	0.50	0.50
MgO	0.85	0.85	0.50	0.85	0.50	0.50
Cl *1	0.85	0.85	0.50	0.85	0.50	0.50
CO_2 *2	0.85	0.85	0.50	0.85	0.50	0.50

*1 The degree of reaction of the limestone filler is assumed to be 50%. Any excess of limestone filler will appear as calcite in the thermodynamic calculations in PHREEQC. Results are consistent with studies in [25].

3.2 Case studies (comparison with experimental data)

The model input parameters for the case studies, including a comparison between numerical results and experimental data, are presented. The specimen names are the same as those used in the corresponding publications, i.e., [24,28]. The following specimens are simulated:

Mortar specimens from the laboratory data [24] simulated in this report comprise:

- Specimen "P": mortar made with white Portland cement (wPC).
- Specimen "M": mortar made with white Portland cement (wPC) with 31.9%-wt. metakaolin (MK).
- Specimen "ML": mortar made with white Portland cement (wPC) with 25.5%-wt. metakaolin (M.K.) and 6.4%-wt. limestone (LL).

Concrete specimens from the field study [28] comprise the following concrete beams:

- Beam "B": concrete made with Portland cement (PC) with 4%-wt. silica sume (SF).
- Beam "E": concrete made with Portland cement (PC) with 20%-wt. fly ash (FA) and 4%-wt. silica fume (SF).
- Beam "F": concrete made with Portland cement (PC) with 12%-wt. silica fume (SF).

3.2.1 Mix-design parameters and binder blends

The mix-design compositions considered as input parameters for the model are shown in Table 6. The assumed oxide compositions used for the case studies are shown in Table 7 and are based on the data in [24,28]. The assumed degree of reaction for the oxides and main components used for the case studies are shown in Table 8.

Table 6 Assumed mix-design used in the case study. Units specified in the table

Property	Laboratory data [24]				Field data [28]			
	Units	P	M	ML	Units	Beam B	Beam E	Beam F
w/b	-	0.5	0.5	0.5	-	0.414	0.417	0.414
Binder content	%-wt.	35	35	35	kg/m^3	387.9	399.4	445.8
Aggregate content	%-wt.	50	50	50	kg/m^3	1832	1834	1722
Air *1	%-vol.	2	2	2	%-vol.	5	5	5

*1 Air contents are estimated.

Table 7 Assumed oxide composition for binder blends used in the case studies. Units in %-wt.

Oxide / element	Laboratory data [24]			Field data [28]		
	P	M	ML	Beam B	Beam E	Beam F
CaO	67.01	45.64	49.12	60.95	51.58	56.60
SiO_2	22.10	32.08	28.92	23.57	29.50	28.83
Al_2O_3	3.61	15.21	12.68	4.66	7.84	4.40
Fe_2O_3	0.24	0.61	0.53	3.37	3.93	3.14
SO_3	3.42	2.34	2.34	2.70	2.35	2.50
K_2O	0.44	0.62	0.56	1.00	1.11	1.00
Na_2O	0.04	0.04	0.05	0.30	0.52	0.28
MgO	1.12	0.91	0.91	2.13	2.06	2.01
Cl *[1]	0.003	0.003	0.003	0.06	0.05	0.06
CO_2 *[2]	2.03	2.53	4.89	1.25	1.40	1.16
TOTAL	100	100	100	100	100	100

*[1] Cl content calculated as NaCl equivalent, *[2] CO_2 values are adjusted based on expected phase assembly from modern binders and LOI values given in the publications.*

Table 8 Assumed maximum degree of hydration for the main oxides of the blends considered for the case studies, expressed as a ratio.

Oxide / element	Laboratory data [24] *[1]			Field data [28]		
	P	M	ML	Beam B	Beam E	Beam F
CaO	0.80	0.80	0.80	0.85	0.84	0.85
SiO_2	0.80	0.65	0.70	0.85	0.72	0.85
Al_2O_3	0.80	0.45	0.45	0.85	0.65	0.85
Fe_2O_3	0.50	0.50	0.50	0.50	0.50	0.50
SO_3	0.80	0.80	0.80	0.85	0.83	0.85
K_2O	0.80	0.80	0.80	0.85	0.74	0.85
Na_2O	0.80	0.80	0.80	0.85	0.75	0.85
MgO	0.80	0.80	0.80	0.85	0.79	0.85
Cl	0.80	0.80	0.80	0.85	0.85	0.85
CO_2	0.80	0.80	0.80	0.85	0.85	0.85

[1] The degree of hydration of the oxides is fixed throughout the whole exposure time, adjusted according to the data shown in [24].

The initial tortuosity factor describes the impact of porosity (and potentially other properties not accounted for). The applied values given in Table 9 were determined by fitting to the experimental data.

Table 9 Initial tortuosity factors determined by fitting to experimental data

Parameter	Unit	Laboratory			Field		
		P	M	ML	Beam B	Beam E	Beam F
Initial tortuosity factor (T_0)	-	1/100	1/1000	1/500	1/100	1/1000	1/500

3.2.2 Exposure conditions

The exposure conditions for the laboratory exposure case study comprised continuous ponding (i.e. fully immersed) of cylindrical mortar specimens with a 2.5M NaCl solution in distilled water [24]. The

specimens were exposed to the solution on one face (i.e. the other specimen faces were sealed), and the solution was replaced regularly. Therefore, in the model 1-dimensional transport with a constant solution composition was assumed. The ionic composition of the exposure media was calculated in PHREEQC and is shown in Table 10.

The exposure conditions for the field study comprised complete immersion in seawater of prismatic concrete beams at approx. 1.5m depth. The samples evaluated in [30] were extracted from the centre of the beam in the submerged part. Thus, 1-dimensional transport is assumed from the two faces exposed to the seawater. The ionic composition of the exposure media for the field study was calculated in PHREEQC, using the input data presented in Table 11. The calculated ionic concentrations, given in Table 12, are utilized as boundary conditions in subsequent simulations.

Table 10 Dissolved species in laboratory exposure solution, calculated from input in [24].

Dissolved species	Concentration ($mmol/kg_w$)
OH^-	2.70E-07
H^+	1.20E-08
O_2	2.00E-05
Na^+	2.50E+00
CO_2	3.53E-05
Cl^-	2.50E+00

Table 11: Elemental composition and basic parameters of seawater.

Element	Ref	Units	Seawater (0 m)	Seawater Average (-20m)
Ca	[23]	$mmol/kg_w$	8.76	8.76
Na	[23]	$mmol/kg_w$	411	411
Cl	[23]	$mmol/kg_w$	548	548
K	[23]	$mmol/kg_w$	8.9	8.9
Mg	[23]	$mmol/kg_w$	46.7	46.7
S	[23]	$mmol/kg_w$	26.9	26.9
O_2	[29]	$mmol/kg_w$	3	5*[2]
Other				
Alkalinity *[1]	[29]	$mmol/kg_w$	2.32	2.31
pH *[1]	[29]		8.1	8.0
Pressure *[3]		atm	1	≈3
Temperature	[29]	°C	2 - 18	7.5

*[1] The composition of the solution is adjusted to the alkalinity and pH values given. The carbon dioxide content in the water is adjusted as HCO_3^- equivalent.

*[2] Average dissolved O_2 concertation is adjusted based on input from [29] and reaching a Redox potential in the couple (O^{-2}/O) of 0.8V.

*[3] The pressure is estimated approximating the hydrostatic pressure of seawater to pure water (i.e. hydrostatic pressure in seawater at -20m ≈1.98 is approximated to 2).

Table 12 Dissolved species in seawater, calculated from input in Table 11.

Dissolved species	Concentration (mol/l)	Dissolved species	Concentration (mol/l)
OH^-	3.1E-07	$Mg(CO_3)$	2.2E-05
H^+	1.0E-08	$Mg(HCO_3)^+$	1.3E-04
O_2	2.3E-03	NaOH	6.1E-08
$Ca(OH)^+$	6.6E-09	Na^+	4.8E-01
Ca^{+2}	7.0E-03	$Na(SO_4)^-$	6.1E-03
$CaSO_4$	8.4E-04	$NaCO_3^-$	3.9E-05
$CaCO_3$	4.6E-06	$NaHCO_3$	1.3E-04
$Ca(HCO_3)^+$	2.1E-05	SO_4^{-2}	1.3E-02
K^+	8.8E-03	HSO_4^-	2.0E-09
KOH	4.3E-10	CO_2	1.8E-05
KSO_4^-	1.4E-04	CO_3^{-2}	9.6E-06
$Mg(OH)^+$	1.6E-06	HCO_3^-	9.4E-04
Mg^{+2}	4.0E-02	Cl^-	5.5E-01
$Mg(SO_4)$	6.5E-03		

3.2.3 Basic model input parameters

A summary of basic input parameters for the model (comprising spatial and temporal resolution, boundary conditions for temperature and pressure, and initial tortuosity factor) to simulate laboratory and field case studies are shown in Table 13.

Table 13 Input parameters used in the laboratory case studies.

Parameter	Unit	Laboratory			Field		
		P	M	ML	Beam B	Beam E	Beam F
Total distance	mm	50	50	50	75	75	75
Total time	days	3	3	3	75	75	75
Temperature	°C	25	25	25	25	5	5
Pressure	atm	1	1	1	1	1	1
Initial tortuosity factor (T_0) *1	-	1/100	1/1000	1/500	1/100	1/1000	1/500

*1 *Parameter determined by fitting*

3.3 Parametric study

Additional input model parameters for the parametric study are described in the following, while additional information is provided in Appendix 2. For the parametric study, the "binder system" group and "Ionic transport" were varied within the ranges shown in Table 14 while the remaining parameters were kept constant.

Table 14 Varied modelling parameters

Parameter Group	Parameter	No. steps	Range
Binder system	Replacement type	3	PC + (FA-SF) PC + (MK) PC + (FA-SF-LL)
	Replacement level	3	0 - 40%-wt. (5%-wt. steps)
	Water/binder	1	Fixed (0.35)
Ionic transport	Initial tortuosity factor	5	1/5000, 1/1000, 1/500, 1/200, 1/100

3.3.1 Mix-design parameters and binder blends

The mix-design composition considered as input parameters for the parametric study is shown in Table 15. For all the simulations, the volume of cement paste (i.e. binder and mixing water) is maintained constant at 25%-vol., considering a fixed water-to-binder ratio of 0.35. The binder blends used for the parametric study are shown in Table 16. The oxide compositions used as input for the model calculations are shown in Table 17. The degree of hydration of the oxides was estimated from Table 2.

Table 15 Mixed-design used in the model verification study.

Property	Units	Value
w/b	-	0.35
Binder content *1	kg/m^3	350
Total aggregate content	kg/m^3	1969
Total aggregate volume	%-vol.	70
Air	%-vol.	5

*1 *The binder content is adjusted to maintain a constant cement paste volume (i.e. considering a constant volume of aggregate, entrained air, and cement paste). The values presented in the table (shown in kg/m3) are approximate.*

Table 16 Cementitious blends considered for the parametric study. Units in %-wt.

Blend ID	Portland (PC)	Fly ash (FA)	Silica fume (SF)	Metakaolin (MK)	Limestone (LL) *[1]
01	100				
02	95		5		
03	90		10		
04	85	15			
05	80	15	5		
06	75	15	10		
07	70	30			
08	65	30	5		
09	60	30	10		
10	90			10	
11	80			20	
12	70			30	
13	85	12.5			2.5
14	80	12.5	5		2.5
15	75	12.5	10		2.5
16	70	25			5
17	65	25	5		5
18	60	25	10		5

*[1] Replacement levels of FA and MK with LL, to 15%-wt. Based on the work in [48]

Table 17 Oxide composition of the blends considered for the parametic study. Units in %-wt.

Blend ID	CaO	SiO_2	Al_2O_3	Fe_2O_3	SO_3	K_2O	Na_2O	MgO	NaCl	CO_2
01	62.21	20.57	4.81	3.46	3.51	0.93	1.09	2.21	0.07	1.15
02	59.11	24.40	4.62	3.29	3.33	0.93	1.04	2.12	0.07	1.09
03	56.00	28.23	4.43	3.12	3.16	0.94	0.99	2.03	0.06	1.03
04	53.63	26.12	7.78	3.99	3.08	1.04	1.18	2.14	0.06	0.98
05	50.52	29.95	7.59	3.82	2.90	1.05	1.13	2.05	0.06	0.92
06	47.41	33.79	7.40	3.65	2.73	1.05	1.08	1.96	0.05	0.86
07	45.04	31.67	10.76	4.52	2.65	1.16	1.27	2.07	0.05	0.80
08	41.93	35.51	10.57	4.35	2.48	1.17	1.22	1.98	0.05	0.75
09	38.83	39.34	10.38	4.18	2.30	1.17	1.17	1.89	0.04	0.69
10	56.01	23.84	8.31	3.26	3.16	0.94	0.98	2.04	0.06	1.39
11	49.82	27.12	11.82	3.05	2.82	0.94	0.88	1.86	0.06	1.64
12	43.62	30.39	15.32	2.85	2.47	0.95	0.78	1.69	0.05	1.88
13	54.86	24.78	7.18	3.82	3.06	1.00	1.14	2.11	0.06	1.99
14	51.76	28.61	6.99	3.65	2.89	1.01	1.09	2.02	0.06	1.93
15	48.65	32.45	6.80	3.48	2.71	1.01	1.04	1.93	0.05	1.88
16	47.51	28.99	9.54	4.18	2.62	1.08	1.19	2.00	0.05	2.83
17	44.40	32.83	9.35	4.01	2.45	1.08	1.14	1.91	0.05	2.78
18	41.30	36.66	9.16	3.84	2.27	1.09	1.09	1.82	0.04	2.72

Table 18 Degree of hydration (maximum) for the main oxides of the blends considered for the parametric study, expressed as %.

Blend ID	CaO	SiO_2	Al_2O_3	Fe_2O_3	SO3	K_2O	Na_2O	MgO	NaCl	CO_2
01	85	85	85	50	85	85	85	85	85	85
02	85	85	85	50	85	85	85	85	85	85
03	85	85	85	50	85	85	85	85	85	85
04	85	73	68	50	84	76	77	81	85	85
05	84	75	68	50	84	76	77	80	85	85
06	84	76	68	50	84	77	77	80	85	85
07	84	66	61	50	82	70	71	76	85	85
08	84	68	61	50	82	70	70	76	85	85
09	84	70	60	50	82	70	70	75	85	85
10	85	77	68	50	85	81	85	84	85	76
11	85	71	61	50	85	78	85	83	85	70
12	85	67	58	50	85	74	84	82	85	65
13	84	75	70	50	84	78	78	81	85	67
14	84	76	70	50	84	78	78	81	85	67
15	84	77	69	50	84	78	78	81	85	66
16	82	67	62	50	83	71	72	77	85	60
17	82	69	62	50	83	71	72	77	85	59
18	82	71	61	50	82	71	71	76	85	59

3.3.2 Exposure conditions

The exposure conditions considered for the parametric study are the same as those used for the field exposure case study, shown in Table 12.

3.3.3 Basic model input parameters

Modelling parameters describing the model setup are summarised in Table 19. The input parameters are grouped into input sets required by the model. Only the "binder system" group and "Ionic transport" are varied in this study. A complete list of input parameters is shown in Appendix B. Selected range of parameters is based on the binder combinations used in parallel investigations of the "*Fergefri E39*" project (see appendix C) and the range of initial tortuosity factor values (calibrated through case studies, see section 3.2 and 4.1).

Table 19 Modelling parameters used for the parametric study

Parameter	Range
Domain length	1 m
Mesh size	(Refined mesh at 0 - 0.5m)
Total time	200 years
Time stepping	(1-year steps)
Moisture transport	Not incl.
Degree of saturation	Enforced (Submerged [1)])
Porosity	Indirectly (calculated from fixed input)
Chemical system	Fixed
Transport mechanism	Diffusion
Temperature	5C
Pressure	1 atm

[1)] *Gradual (linear) increase in the degree of saturation over time is assumed: from 80%$_{-vol.}$ at t=0 to full saturation (99%$_{-vol}$).*

4. RESULTS

This chapter contains the results from the numerical investigations carried in this study. Numerical results can be accessed in [33].

4.1 Comparison to experimental data (case studies)

This section includes the results from the comparison of model and experimental data. The section presents results from two sets of experimental data:

- Results from the comparison with laboratory data, see also [24]
- Results from the comparison with field data, see also [28]

4.1.1 Comparison to laboratory data

The chloride profiles from the modelled results are compared to the experimental laboratory data in Figure 3. The figure shows the measured and calculated total chlorine content (expressed as %-wt.) in the outermost 25 mm of the modelled domain. The modelled data were calculated for four levels of the total physical binding capacity of the C-S-H (0%, 30%, 60% and 100%), for calibration purposes. These four cases were studied to calibrate the total binding capacity parameter (γ) of the Langmuir binding model shown in Eq. 6.

Results from the case study made with only white Portland cement (i.e. specimen "P" in Figure 3a) show a close fit between the model and experimental data. Changes in the total binding capacity had a moderate impact on the total predicted bound chloride, the impact was most pronounced at the surface. The data indicates that the cases considering a 30-60% binding capacity reached the best agreement with the experimental data. Results from the simulations of Portland cement blended with metakaolin (i.e. specimens "M" and "ML" in Figure 3b-c) showed a larger binding capacity compared to the measured one in the experiments, regardless of the binding capacity considered (see higher predicted values at the outermost 2mm in Figure 3b-c). Limited variation in the total chloride profile (after 1mm) was found for a binding capacity of up to 60%. Initial tortuosity factors were determined by fitting to be 1/100 for P, 1/1000 for M, and 1/500 for ML:

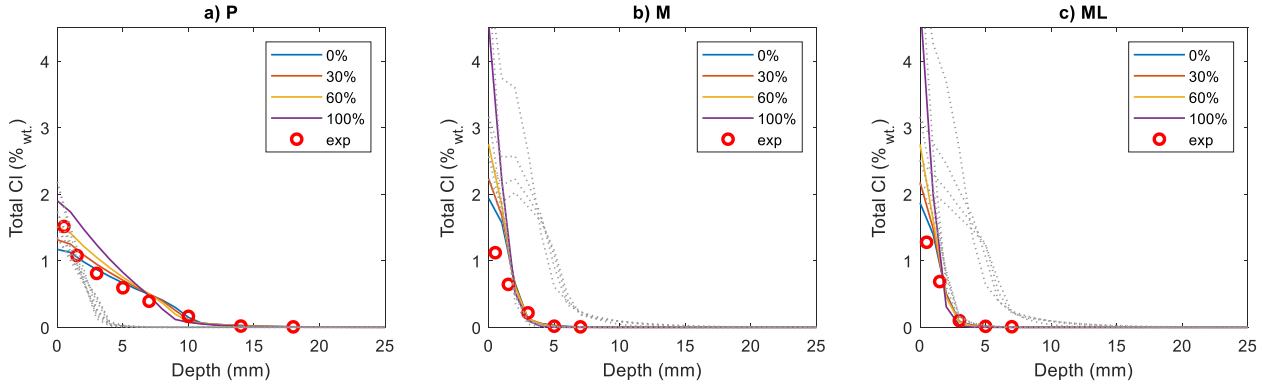

Figure 3 Comparison of model results and experimental laboratory data for mortar specimens made with: a) white Portland cement (P), b) white Portland cement and metakaolin (M), and c) white Portland cement, metakaolin, and limestone (ML). Total chlorine mass per total weight expressed in $\%_{wt}$. The amount of C-S-H allowed to adsorb free chloride from the solution was varied in the simulations (shown in the legend). Broken lines represent the profiles calculated for each material using the initial tortuosity input factor of the other two materials (i.e. to show indicatively the role of the tortuosity factor).

4.1.2 Comparison with field data

The chloride profiles from the modelled results are compared to the experimental field data in Figure 4. The figure shows the measured and calculated total chlorine content (expressed as $\%_{wt.}$) in the outermost 25 mm of the modelled domain. The modelled data were calculated for three levels of the total binding capacity of the C-S-H (i.e. 30%, 60% and 100%), which are shown in the legend.

It is observed that for the concrete mixes without fly ash (e.g. Beam B and F in Figure 4a and c), the predicted amount of total bound chloride is significantly smaller than the measured values. Whereas for the concrete mix with fly ash (e.g. Beam E in Figure 4b), already the chemically bound chloride appears to exceed the total amount of bound chloride, as shown by the limited increase in the bound chloride when increasing the total binding capacity of the C-S-H. These observations regarding the uncertainty of predictions of the total amount of bound chloride are consistent with the observations made for the laboratory exposed specimens (see Figure 3), i.e. the specimens containing metakaolin also reached much higher total chlorine, regardless of the total binding capacity considered for the C-S-H (i.e. as physical binding). It is observed that, for the cases where no SCMs are used (e.g. Figure 4a,c and Figure 3a), the amount of bound chloride increases substantially when increasing the binding capacity of the C-S-H, even at the tail (i.e. up to approx. 70mm deep in Figure 4a). The contribution from the physically bound chloride to the total bound chloride predicted on the binder containing metakaolin (Figure 3b-c) or fly Ash (Figure 4a,c) is large at the surface, but does not have such an effect at the tail.

Initial tortuosity factors were determined by calibration. Comparable modelled and measured ingress depth were obtained using 1/100 for Beam B, 1/1000 for Beam E, and 1/500 for Beam F as input.

The phase assemblage of the exposed cement paste after 25-years is shown in Figure 5 for:

a) the beam with Portland cement and 5% silica fume (see Beam B Figure 5a), and
b) the beam with Portland cement and fly ash (Beam E in Figure 5b).

The model results show, for both cases, a substantial alteration of the phase-assemblage in the outermost 10 mm after 25-years of exposure. The results also show a reduction of the overall porosity in the outermost 5-10 mm, mainly due to the formation of ettringite and thaumasite at the surface. The formation of Friedel's and Kuzel's salt is more pronounced in the concrete blend including fly ash (see beam E in Figure 5b). No experimental data for the actual concretes were available for comparison.

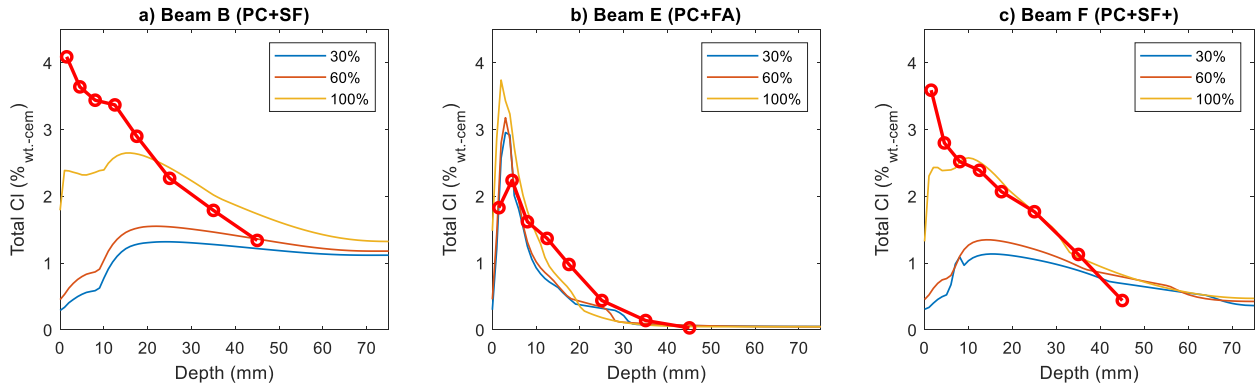

Figure 4 Comparison between modelling results and experimental data, i.e. the total chlorine mass per binder weight, expressed in $\%_{wt\text{-}cem}$. The amount of C-S-H allowed to adsorb free chloride from the solution was varied in the simulations (shown in the legend).

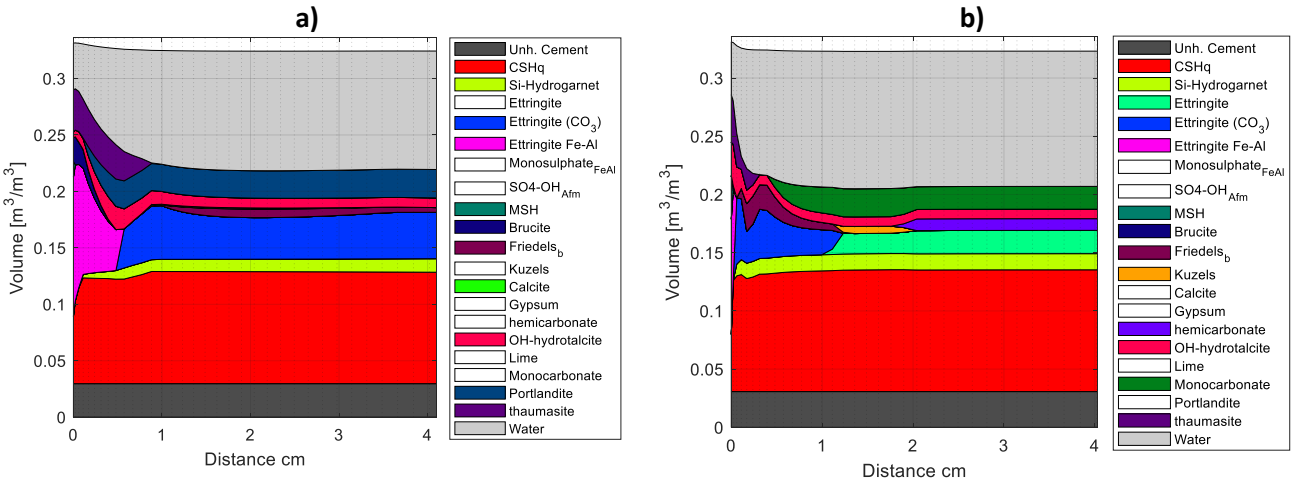

Figure 5 Phase assemblage of modelled field data after 25-years exposure, for a) Beam B and b) Beam E.

4.2 Parameter study

The parameter study results comprise 90 simulations corresponding to the blend IDs shown in Table 16. The objective of the parameter study was to produce a set of data that describes the relevant model results for the prediction of corrosion initiation, namely: total chlorine content, pH, chloride concentration in the pore solution; and a combination of the two latter: the $[Cl^-]/[OH^-]$ ratio. These results lead ultimately to a prediction of the cover thickness associated with relevant threshold values for corrosion initiation. All data are available in [33]. An example of the output data is further analyzed in section 4.3 for all the model runs.

Figure 6 shows the phase assemblage and ionic composition of the pore solution after 200 years of exposure for blend 01, i.e. the reference blend with 100% Portland cement and an initial tortuosity factor of 1/500. It should be noted that the assumed initial tortuosity factor is lower than found in the case studies, which results in a lower ingress depth (compare full and dotted lines in Figure 3).

Figure 7 shows the variation of the total pore volume over time, derived from the phase assemblage data presented in Figure 6. The data presented in Figure 7a shows the variation of porosity over the depth and time in a 2-dimensional plot. Figure 7b shows the same information at discrete spatial points over time. The changes to the pore volume (and pore connectivity) result in changes in the transport properties, which is illustrated as the time-dependent change in tortuosity factor relative to t=0 in Figure 7c. It should be kept in mind that there is an inverse (non-linear) relation between the tortuosity and the total pore volume (e.g. see section 2.2.1). In the example shown in Figure 7a-b, it can be observed that reduction of the bulk paste porosity (due to hydration) is moderate and occurs mainly during the first 20-years. In contrast, , the reduction of porosity at the surface (i.e. due to interaction with the environment, see Figure 6a) is more pronounced (see Figure 7b). The predicted reduction of the total pore volume over time causes a substantial reductions of the tortuosity factor (i.e. expected increasing tortuosity at pore structure) in the outermost 20 mm in Figure 7c. It should be mentioned that recent field studies are in contrast to these observations of densification, which call for further investigations.

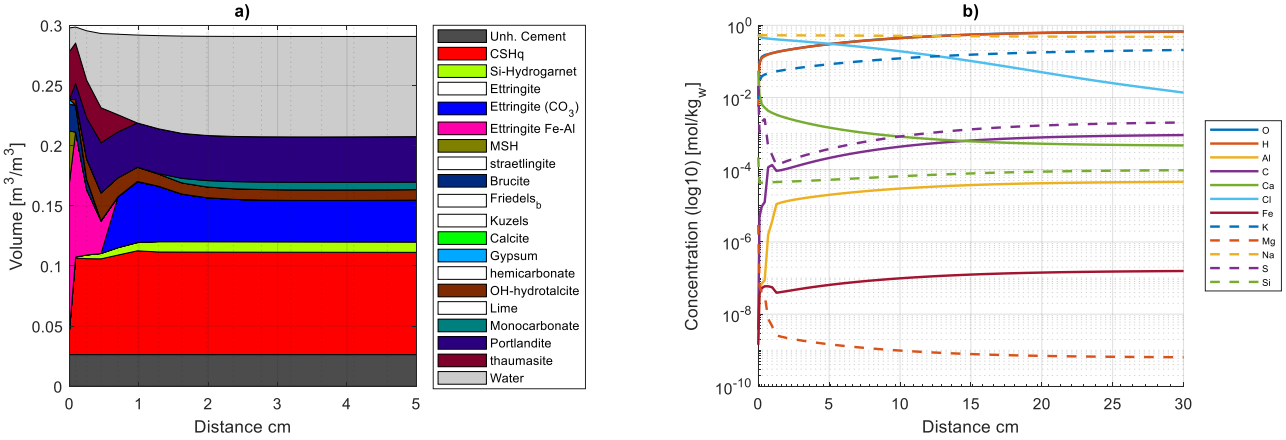

Figure 6 Selected modelling results for blend 01 (see Table 16) illustrating a) phase assemblage (in the outermost 50 mm) and b) elemental composition of the pore solution. (results at 200 years)

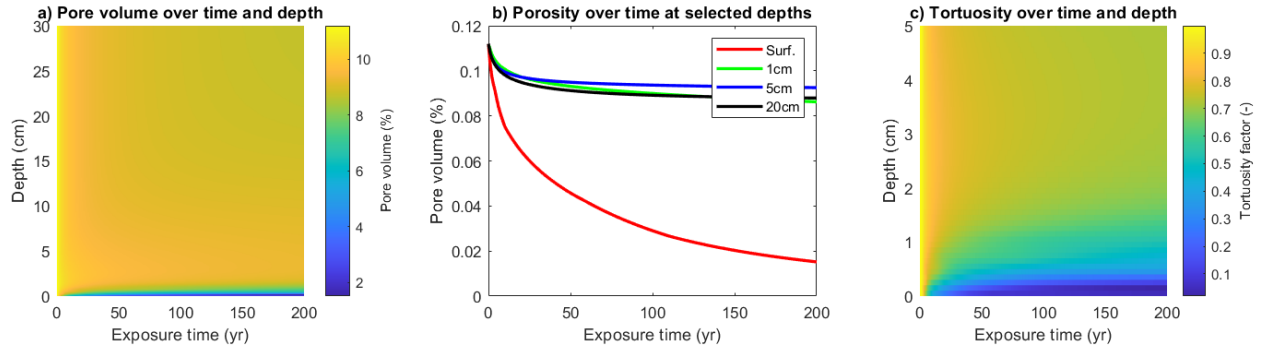

Figure 7 Selected modelling results for blend 01 (see Table 16) showing total pore volume, expressed in %-vol, dependent on a) exposure time and depth, b) exposure time at selected depths; and c) relative tortuosity factor (compared to t=0) in the outermost 5cm.

Figure 8 shows selected model results relevant for the initiation of reinforcement corrosion. Results are plotted for the following parameters:

- The free chloride concentration in the pore solution expressed in mol/l (see Figure 8a)
- The total chlorine concentration in the pore solution (see Figure 8b)
- The pH of the pore solution (see Figure 8c)
- The free chloride to hydroxyl ion ratio $[Cl^-]/[OH^-]$ (see Figure 8d)

Selected threshold values for each parameter (not pH) are marked and plotted in red, applying different thresholds for corrosion initiation (see values inTable 1). The depth of threshold boundary (in red) at each point in time will be used in the following sections to calculate the cover thickness required to prevent corrosion initiation of steel reinforcement at each point in time. The graph can be used directly to reference the expected ingress-depth at which corrosion of reinforcing steel may occur (i.e. depending on the threshold parameter and value selected). The results shown in Figure 8 highlight the impact of selecting a relevant threshold parameter (and corresponding values) to describe the initiation of reinforcement corrosion. Consideration of "traditionally used parameters" such as the total chlorine content per binder weight may be compared directly to more coherent parameters, e.g. the free chloride ion concentration in the pore solution or the chloride to hydroxyl ratio

[20]. The data also highlights the immense impact of selecting a threshold value that significantly impacts the predicted cover depths and is known to have a large variability [20].

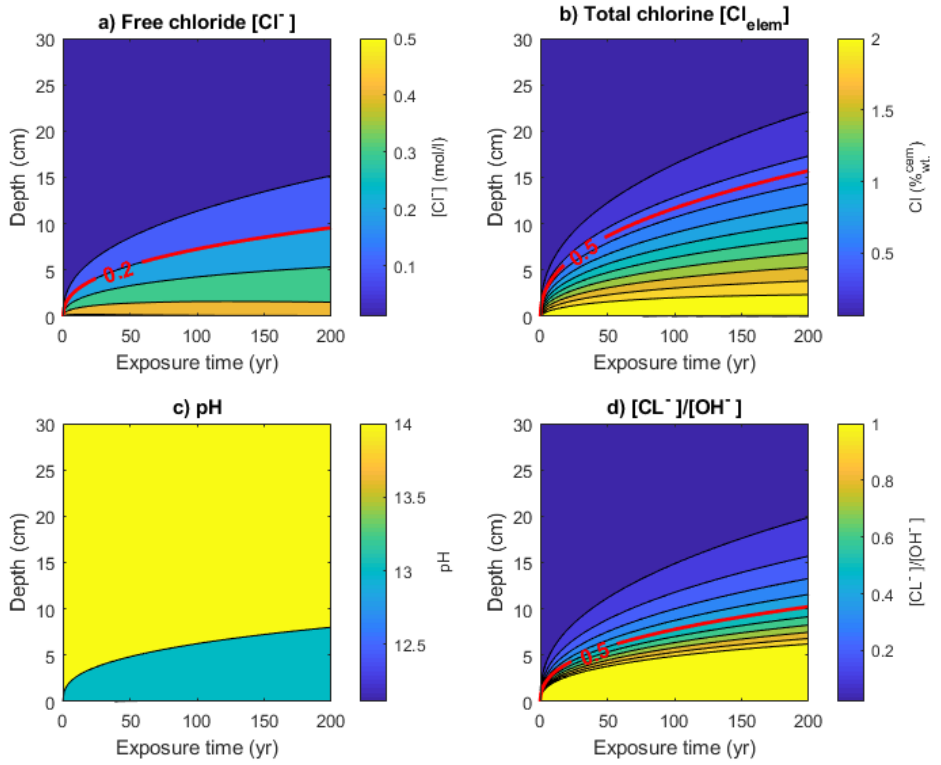

Figure 8 Selected modelling results as a function of depth for blend 01 (see Table 16) illustrating a) free chloride [Cl^-] in solution in mol/l, b) the total amount of chlorine in the whole system in %-wt. cem, c) pH of the pore solution, and d) the ratio of the concentration of free chloride to hydroxyl in solution [Cl^-]/[OH^-]. The threshold values suggested in Table 1 are indicated by red lines

4.3 Regression model results

This section presents the results from a regression modelling of the simulated data produced in the parameter study. Two regression models were investigated:

1. A multilinear regression model, based on the Partial Least Square Regression method (PLS), was used to quantify the "weight" of the study parameters (i.e. explanatory variables) in the model response (e.g. the minimum cover thickness for a service life of 200 years).
2. A machine-learning-based regression model, i.e. a Gaussian Process Regression (GPR) model, was used to interpolate within the initially computed dataset to produce a graphical representation of the interpolated data.

4.3.1 Partial Least Square Regression method (PLS)

The Partial Least Square (PLS) regression method was used to quantify the impact of the model parameters on the prediction of the minimum cover for the reinforcement (i.e. to prevent initiation of reinforcement corrosion). The PLS model was used as a sensitivity study of the main model parameters within a reasonable range (i.e. based on the ranges selected in the study). The model input parameter range was selected based on the input parameters investigated in the case studies, see Table 20. The response variable, i.e. the minimum cover thickness after 200 years to prevent initiation of reinforcement

corrosion, was calculated considering the highest resulting cover value for the four threshold parameters selected for corrosion initiation in Table 20.

The resulting weight of the main variables on the response variable (i.e. the cover thickness after 200-years of exposure) is shown in Figure 9. The explained variance and residual plots, Figure 9a and Figure 9b, respectively, show a modest fit of the regression model to the synthetic data, which explain approx. 60% of the variance with a single component (i.e. most of the variation in the resulting cover can be explained in one dimension; therefore, there is a linear dependency between most of the variables and the calculated cover thickness). The resulting weight of the main model parameters for the first six principal components is shown in Figure 9c. The figure shows that with the parameter ranges studied, the threshold values selected have a normalized weight of approximately 50%. Among these, it is worth noting that the total amount of chlorine by weight of binder (unit typically used in performance-based durability design methods) represents approximately 50% of the total weight of the threshold values. The overall binder composition had a normalized weight of approximately 20% on the resulting cover estimation. In contrast, the initial tortuosity factor had a relative weight of approximately 30%. It shall be remarked that the initial tortuosity factor and binder selection are tightly related since the effective transport of ions is governed by the microstructure of the pore system, which is (but not exclusively) defined by the chemical and physical (i.e. particle size distribution) characteristics of the binder (e.g. binder composition and degree of hydration).

The second set of calculations was made where only the $[Cl^-]/[OH^-]$ ratio was considered as the threshold value (see Figure 10). The explained variance and residual plots show a substantially better fit of the regression model to the synthetic data compared to the previous regression model. In this case, the regression model can explain approximately 80% of the variance within the first three components. The resulting weight of the main model parameters for the first six components is shown in Figure 10c. The figure shows that the corrosion threshold has a normalized weight of approximately 35% with the parameter range studied. The overall binder composition had a normalized weight of approximately 40% on the resulting cover estimation. At the same time, the initial tortuosity factor had a relative weight of approximately 25%. These changes of the relative weights indicate that the predicted covers are now more sensitive to variations in the pH of the pore solution, which are primarily governed by the chemical composition of the binder system.

Table 20 Investigated parameter range in PLS study

Parameter	Lower bound	Upper bound	Units
Model			
Initial tortuosity	1/100	1/10000	-
Portland cement	60	100	%-wt.
Fly ash (FA)	0	30	%-wt.
Silica fume (SF)	0	10	%-wt.
Metakaolin (MK)	0	30	%-wt.
Limestone (LL)	0	5	%-wt.
Threshold values			
pH	8	11	
$Cl_{elem.}$	0.4	2.0	$\%\text{-}wt_{bw}$
$[Cl^-]$	0.3	2.0	mol/kg_w
$[Cl^-]/[OH^-]$	0.2	5	-

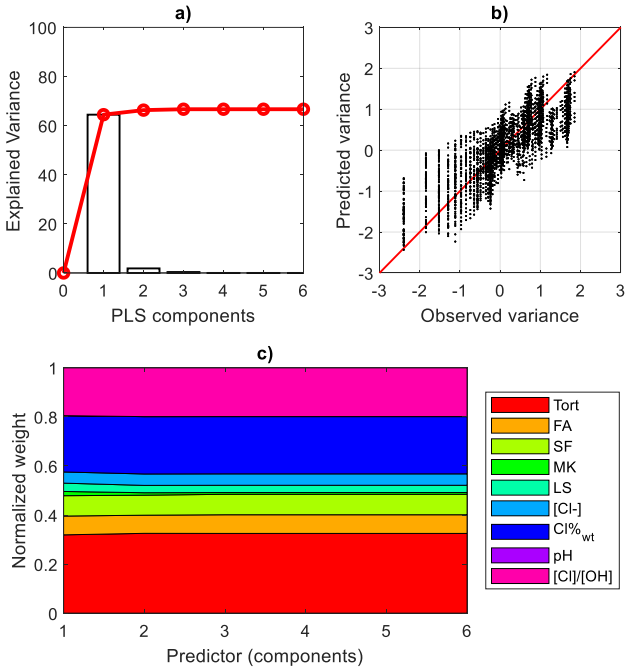

Figure 9 PLS regression model results including all threshold values, showing a) the explained variance by the first 6 model components, b) the residual plot, and c) the normalized weight of the model variables with an increasing number of principal components.

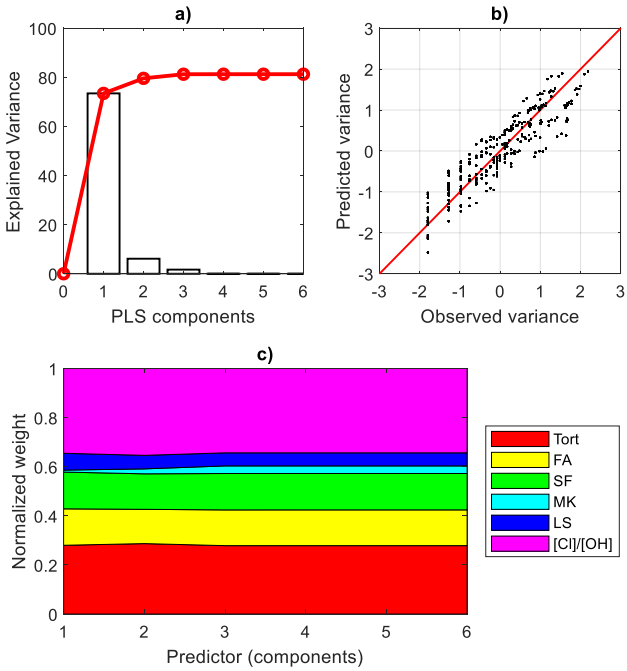

Figure 10 PLS regression model results considering $[Cl^-]/[OH^-]$, showing a) the explained variance by the first 5 model components, b) the residual plot, and c) the normalized weight of the model variables with an increasing number of principal components.

4.3.2 Machine-learning based regression model

A machine-learning-based regression model (based on an ensemble-tree model [49–51]) was trained with the results from the parameter study (i.e. synthetic data). The model was used to interpolate the synthetic data to show the various interactions between the main variables studied graphically. The investigated ranges and default values are given in Table 21. It should be mentioned that the initial tortuosity factors are low compared to very dense concretes, i.e. lower bound compared to initial tortuosity factors determined for the densest cases (see, e.g. mortar M, Section 4.1.1 and Beam E, Section 4.1.2). Selected model results are plotted in Figure 11-14. The results show the critical cover thickness in a colour contour for various input parameters in the x- and y-axes.

Table 21 Investigated parameters in the Machine-learning study

Parameter	Lower bound	Upper bound	Default value *1	Units
Model				
Initial tortuosity factor	1/100	1/5000	1/1000	-
Fly ash (FA)	0	30	15	%-wt.
Silica fume (SF)	0	10	5	%-wt.
Metakaolin (MK)	0	30	0	%-wt.
Limestone (LL)	0	5	0	%-wt.
Threshold values				
pH	8	11	9	
$Cl_{elem.}$	0.4	2.0	0.6	$\%\text{-}wt_{bw}$
$[Cl^-]$	0.3	2.0	0.4	mol/kg_w
$[Cl^-]/[OH^-]$	0.2	5	0.5	-

*1 Default values used for the comparison of threshold values and initial tortuosity factor.

Figure 11 shows the variation of the calculated cover thickness, comparing two threshold values considered for corrosion initiation, i.e. the total chlorine content per binder mass (often considered in practice) and the ratio of chloride to hydroxyl ions in solution $[Cl^-]/[OH^-]$. The results show a similar trend for both parameters, i.e. a reasonably linear correlation compared to the ranges investigated.

Figure 12 shows the variation of the calculated cover thickness, considering a binary binder system with fly ash (FA) and silica fume (SF) replacement of the Portland cement (PC). The results in Figure 12a indicate the presence of local minima for the cover thickness at relatively low replacement ratios of FA and SF (see markup in red in Figure 12a). Figure 12b-c show a comparison of the relative impact of the replacement of PC (i.e. with FA and SF) together with the initialtortuosity factor. The figures show that the expected increase in tortuosity due to these additions, i.e. considering the effect on the microstructure (convered implicitely by this model), may compensate for the moderate increase in the cover thickness when increasing these at a fixed tortuosity factor. Thus, values shall be interpreted by looking at the expected trends (indicatied with a red arrow).

Figure 13 shows the variation of the calculated cover thickness, considering a ternary binder system with fly ash (FA), silica fume (SF), and limestone (LL) replacement of the Portland cement. The plots show the synergy between fly ash and limestone at constant silica fume content (5%-wt.) in Figure 13a. The addition of limestone only results in a reduction of the cover thickness at approximately 20%-wt. fly ash replacement. The interaction between the replacement of a 10%-wt. fly ash blend with silica fume and limestone show an overall reduction of the cover when increasing the content.

Figure 14 shows the variation of the calculated cover, considering a binder system with metakaolin (MK) replacement of the Portland cement, compared to fly ash (FA) replacement. The plot shows an overall monotonically decrease in cover thickness with increasing metakaolin replacement, up to

values over 20%-wt. replacement. Whereas there is a local minimum in the calculated cover at approximately 10-15 %-wt replacement of fly ash (e.g. shown with a red dashed line in the figure).

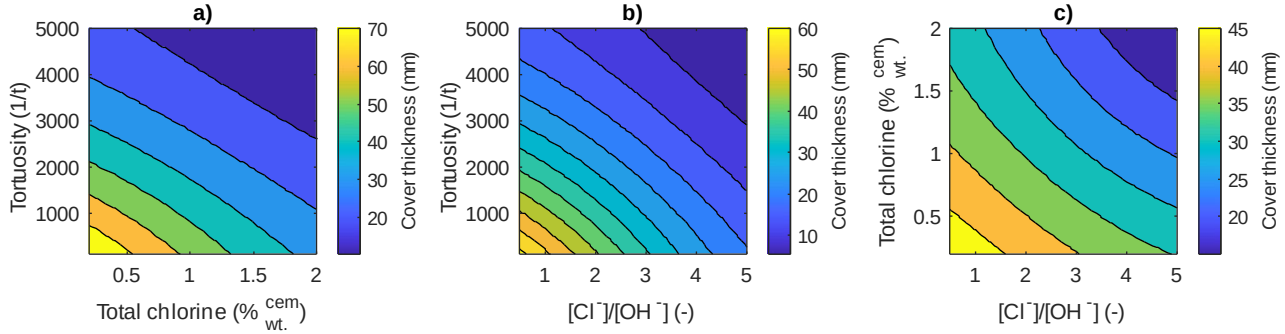

Figure 11 Selected regression model results showing the relation between cover thickness after 200 years of exposure and a) total chlorine threshold vs initial tortuosity factor, b) $[Cl^-]/[OH^-]$ vs initial tortuosity factor, and c) $[Cl^-]/[OH^-]$ vs total chlorine threshold for a fixed initial tortuosity factor (1/2000).

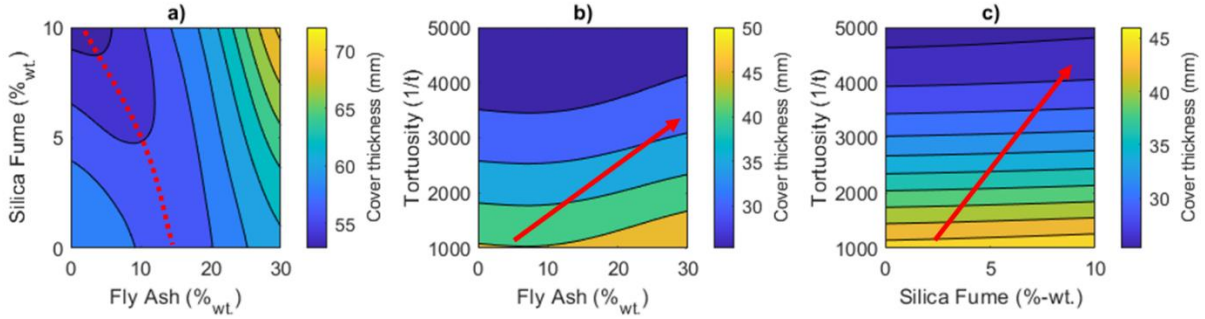

Figure 12 Selected regression model results showing the relation between cover thickness after 200 years of exposure and a) FA and SF content (i.e. at a fixed initial tortuosity factor of 1/1000), b) FA and initial tortuosity factor (5%-wt. SF), and c) SF content and initial tortuosity factor (15%-wt. FA). Expected trends in development of initial tortuosity factor at increasing replacement levels are indicated by red arrows.

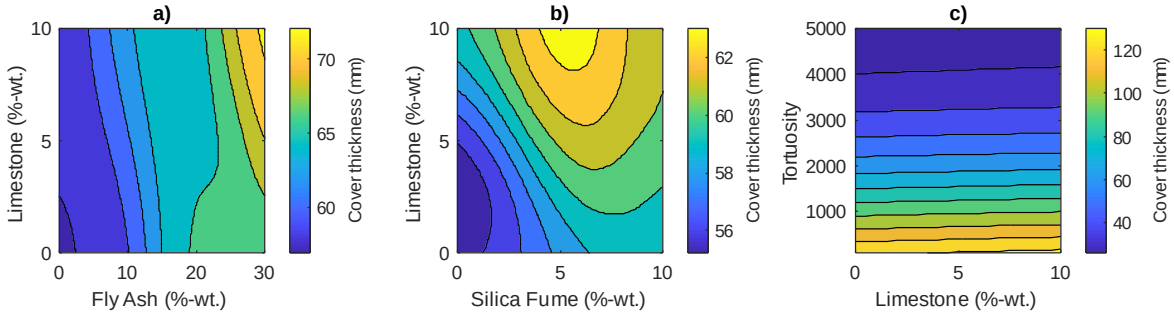

Figure 13 Selected regression model results showing the relation between cover thickness after 200 years of exposure and a) FA and LL content (with 5% SF), b) SF and LL content (with 10% FA), and c) LL content and initial tortuosity factor (with 12.5% FA and 2.5% SF).

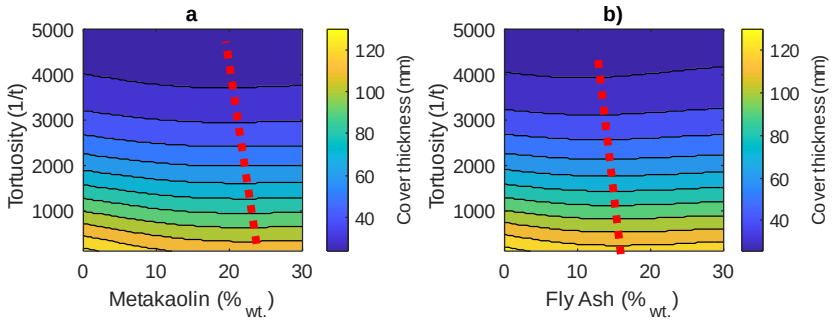

Figure 14 Selected regression model results showing the relation between cover thickness after 200 years of exposure and a) MK content and initial tortuosity factor and b) FA and initial tortuosity factor. The red dashed line indicates a local minimum in the calculated cover at approximately 10-15 %-wt replacement of fly ash.

5. DISCUSSION

This section contains a discussion of the modelling results and focuses on describing the potential advantages and challenges of using an RMT model described herein to predict chloride ingress and corrosion initiation.

The discussion covers: i) the comparison of the model predictions compared to two reference case studies (laboratory exposure of mortar specimens, and coastal exposure in Norway of concrete), including the sensitivity of the model results to input parameters (see 5.1 and 5.2); and ii) the applicability of RMT models to engineering applications within the context of concrete infrastructure service life design considering the combination of RMT models with machine-learning techniques (see sections 5.3 and 5.4).

5.1 Comparison of modelled and experimental data

Overall, trends observed in the phase assemblage of marine exposed concrete agree with results in similar investigations, e.g. [42] (no experimental data were available on the phase assemblages of the field exposed concrete used for the case study). Observations include the precipitation of Mg-rich phases in the outer surface followed by sulphur-rich and carbonate phases and chloride-bearing phases deeper into the domain. In contrast to the modelled densification of the outer surface, laboratory studies [41] indicate no change to the porosity at the surface, while recent field data indicates a porosity increase of up to 1 cm depth after ten years behind a potentially scaled denser surface crust, refer to [52].

The comparison of the modelled and experimental chloride ingress profiles indicates a twofold challenge when modelling chloride ingress in cementitious systems:

- The modelled data showed misleading results compared to the experimental data of chloride binding capacity, particularly when considering the effect of aluminates on the predicted chloride binding capacity.
  - The predicted chloride binding capacity for systems with high aluminium content (e.g. fly ash and metakaolin blends) was too large. The net effect of the chemical binding of chloride (e.g., Friedel's salt) exceeded the measured chloride.
  - The use of semi-empirical models (e.g. the Langmuir isotherm model used in this case) may not fully capture the actual binding mechanisms. A better description of the chloride binding mechanisms may require the use of more advanced electrical double layer models with a more robust physic-chemical basis (e.g. see [32]).
- Simulating the rate of ingress currently involves an experimentally determined tortuosity factor. Transport models for ionic species (chloride ions in this case) do not fully account for the multiscale nature of the problem at the moment. Transport properties of the pore structure and the pore solution's ionic composition are expected to vary at different pore spaces (e.g. capillary vs gel porosity).

These observations highlight the need for additional comparative studies to understand better the impact of the modelling assumptions (e.g. phase assemblage selection) on the expected model results. At present, there is limited availability of detailed datasets tailored to calibrate and verify RMT models under realistic exposure conditions (e.g. for seawater).

5.2 Sensitivity study of model input parameters

The simulation results presented in section 4.3.1 indicate no single governing parameter for the calculated cover to meet 200 years of design service life. The overall weight of the investigated study parameters (e.g. binder composition, initial tortuosity factor and threshold values for corrosion initiation) show that these parameters share similar importance when estimating the minimum cover needed to prevent initiation of reinforcement corrosion. Two of the parameters, initial tortuosity factor and binder

composition, are considered strongly related, yet these relations are not fully captured by the model in its current stage of development (e.g. refer to ongoing work in [19] and [53]).

The contribution of the initial tortuosity factor was lower than expected, although the initial tortuosity factor was varied by a factor of 100 in the simulations (addressed in the parameter sensitivity study). Variations in initial tortuosity factor observed in the case studies were only of a factor of approximately 10. The still moderate impact of the initial tortuosity factor in the overall cover calculation (i.e. approximately 30%) would be substantially smaller if a less conservative range were considered. For example, additional results (not shown in this report, refer to data in [33]) considering a range comparable to the experimental cases simulated (i.e. of 1/100-1/1000) show a relative weight of the initial tortuosity factor of approximately 20% (resulting in an increase of the relative weight of the binder combination and threshold values to approximately 40% each). It is essential to note that for the exposure conditions simulated in this study, the model predicted re-precipitation of phases at the surface of the simulated specimen, which reduced the effective transport of ions in the outermost 5 mm of the spatial domain already at the early stages. The results indicate a reduction of approximately 50% over the first ten years and 80% over the first 25 years (see, e.g., Figure 7c), thus increasing the net chloride ingress resistance towards the reinforcement by approximately 10% at 25 years (e.g., considering a cover of 70 mm). The binder composition is expected to affect the tortuosity, as observed in the comparison of modeled and experimental data (see section 4.1) and supported by previous research [44,54,55]. Mechanisms to describe the tortuosity should also consider potential side-effects, such as the formation of phases at the surface (as discussed above) and further changes to the net ingress of species (e.g., Cl^-).

The observed impact of the initial tortuosity factor suggests that an initial estimate of the tortuosity factor range for the considered mix-designs may be effective to reduce the uncertainty of this parameter in design-oriented simulations, e.g., based on comparison to experimental data measured at an early exposure time.

The binder composition appeared to impact the cover thickness calculations substantially, particularly when considering the $[Cl^-]/[OH^-]$ ratio as a threshold parameter for corrosion initiation. Such observations are consistent with the expected decrease in the pH of the pore solution of blended cement and their lower pH buffer capacity (due to the lower Portlandite content).

Finally, it was observed that the selection of threshold parameters (and threshold values) for initiation of reinforcement corrosion had a substantial impact on the calculated cover thickness, even though the ranges selected comprised only a part of the values reported in [20]. Overall, it was observed that the selection of the type of threshold parameter for chloride-induced corrosion, e.g., considering the total chlorine content vs. the $[Cl^-]/[OH^-]$ ratio, had a significant impact on the relative role of the binder composition. It was thereby observed that the $[Cl^-]/[OH^-]$) is more robust and presents a better explanation of the variance (i.e., a better fit to the synthetic data) in the PLS model.

5.3 Model capabilities

The applied RMT model was capable of producing a comprehensive set of data, and provided a method to predict the initiation of reinforcement corrosion (based on corrosion-initiation threshold values) for a wide variety of cement compositions. The RMT model facilitate the use of threshold parameters as e.g. the [Cl-]/[OH-] ratio at the pore solution instead of the less relevant total chlorine content currently used in engineering design (e.g. see [2,4,9]).

The input parameters required by the model (e.g. binder composition, microstructure (tortuosity), and boundary conditions) are based on physical and chemical parameters that can be retrieved from existing literature or measured. Changes to the boundary conditions of the model over time (e.g. ionic composition of the seawater or temperature) may be simulated based on local climate change and

ocean acidification predictions. Such capabilities are typically not covered by less detailed models, e.g. based on analytical solutions of Fick's law [2].

The data produced (e.g. the predicted phase assemblage, ionic concentration, and pore structure) can be used to evaluate additional chemical deterioration mechanisms of the cement paste that may affect the long-term performance of concrete infrastructure, e.g. sulphate attack, calcium leaching or carbonation. Likewise, the data produced with RMT models can be used to predict further damage induced by reinforcement corrosion in the propagation phase by coupling with reinforcement corrosion models, such as presented in [56].

5.4 Parameter interpolation as a potential design tool

The final part of the study comprised a machine-learning regression model, which was used to interpolate within the parameter study's calculated results and present graphically the trends observed in the calculated cover thickness after 200 years of exposure.

The training process of the regression model with the synthetic data produced by the RMT model was found reasonably fast, e.g. ranging from times below 1 minute for linear or tree models to a few hours for SVM Quadratic models (using approx. 80k observation points). After that, the trained model provided a fast interpolation (e.g. reaching over 50.000 calculations per second on an office laptop). This would allow for the implementation of RMT models in more advanced engineering performance-based design approaches.,

Model predictions were generally bound to the resolution of the (synthetic) input data from the RMT model, so that additional model runs are necessary to produce more detailed machine-learning regression model predictions. However, considering the fast model training process (e.g. taking a few seconds on a standard desktop computer), there is potential for re-training a model with additional data from simulations based on engineering judgment for each application. Thus, allowing an iterative refinement process of the model to identify fewer key parameter combinations in durability-design applications, e.g., by selecting a narrower binder range.

Overall, the regressed data revealed trends regarding the role of the addition of SCMs in binary and ternary blends for a fixed initial tortuosity factor (i.e., 1/1000). As earlier mentioned, the initial tortuosity factors used in the parametric study compare to very dense concretes: 1/1000 used as lower bound compare to initial tortuosity factors determined for the densest cases (mortar M, see Section 4.1.1 and Beam E, see Section 4.1.2).

It should be kept in mind that the results presented are based on a still limited comparison to experimental data, and results shall be regarded as "trends" and subject to further analysis and discussion to be considered for engineering applications. Further comparison with experimental data on a narrower combination of binder blends could be used to provide a more detailed estimation of expected covers.

All in all, the modelling framework presented shows a considerable potential to extend existing service-life models (e.g. *fib* Model Code for Service Life Design [2]). However, further work is still needed, particularly regarding chloride transport and binding in the C-S-H. Among others, recent research results from the ongoing European research project ERICA are expected to provide a valuable basis for such further work.

6. SUMMARY

This report discussed the applicability of reactive mass transport (RMT) models for the durability design of concrete structures. The study focussed on supporting service life modeling of chloride-induced reinforcement corrosion of immersed concrete structures in the Norwegian coastline.

Model results were compared to experimental data of selected case studies for chloride ingress in mortar and concrete mixes. The modeled data showed a relatively good agreement with the experimental results of concrete specimens exposed to seawater in the Norwegian Atlantic coast for 25 years. Model results described well the elemental zonation, but also indicated densification at the exposed concrete surface, which is in contrast to recent fields studies. Comparison of modeled and experimental data also revealed existing model limitations when describing the physical binding of chloride in the C-S-H and the overall impact of tortuosity on ingress rate.

A parametric study was carried out to evaluate the model performance to predict the minimum concrete cover required to avoid chloride-induced corrosion of reinforcing steel in a concrete element immersed in seawater. A sensitivity study covering the main model input parameters was carried out using the Partial Least-Square (PLS) method. The results of the study indicate that the primary model input parameters, i.e., tortuosity of the pore structure (tortuosity factor), binder composition, and corrosion-initiation threshold parameter, have a comparable impact weight on the model predictions for the minimum cover thickness to prevent initiation of chloride-induced corrosion. This indicates that model uncertainty does not solely comprise parameters that must be adjusted (e.g., the tortuosity factor) but also parameters that shall be selected based on engineering judgment.

A machine-learning-based regression model was trained using the parametric study results to provide a fast interpolation method between the parameter study variables. The regression model effectively provided fast and consistent interpolation between the data with approximately 150k observations.

The methodology presented in this study has shown an excellent potential to be implemented in existing performance-based durability models, such as *fib* Model Code 34, where RMT models can provide a robust physically-based transport model to replace existing analytical solutions.

7. FURTHER STUDIES

The following research areas concerning the further development of RMT models and their implementation into practical service life design applications were identified:

Verification of model assumptions and validation of model results with tailored experimental data

Experimental data reported in former studies generally do not focus on validating RMT models, which are generally more complex than existing models. Thus, verification of some of the modeling assumptions is hindered by the level of detail in the input and output data provided. The following aspects need to be addressed in future research:

- Development of tailored experimental campaigns, e.g., at laboratory scale that focuses on crucial modeling aspects, such as the pore structure and microstructural features, the phase assemblage, and the pore-solution composition. For example, an initial estimate of the tortuosity factor range, based on experimental data, may be effective to reduce the uncertainty of this parameter in design-oriented simulations.
- Evaluation of additional case studies from existing structures (or test specimens) under representative field exposure conditions to verify model predictions under realistic design conditionsSuch case studies need to have sufficient detail of information (i.e., particularly concerning input parameters) to reduce the input model uncertainty
- Establishing "best-practice" guidelines for the design of future experimental investigations to ensure that input parameters and results, which are required for model validation, are described coherently and homogeneously and can be utilized to verify and benchmark (more advanced and complex) RMT models.

Implementation of physical binding of chlorides and impact of porosity in RMT models

The RMT model presented herein showed a good agreement with experimental data. However, some aspects related to the physical and chemical binding of chlorides are not fully captured by the model (at the current stage of development); neither is the impact of the connectivity of the porosity, the tortuosity, which is currently based on experimental data. The existing model approach to describe the physical binding (i.e., adsorption) of chlorides in the C-S-H is based on a (simple) isotherm model that needs to be calibrated to experimental data and thus does not provide a robust solution that can be extrapolated to various exposure conditions or binder combinations. Further development of the existing model framework is needed to capture this aspect better:

- Implementation of electrical double layer models into the existing RMT framework to provide a robust physic-chemical basis for the adsorption of chlorides in the C-S-H
    - Such models are already developed in the chemical solver used in this investigation (i.e., Phreeqc) for general applications; however, they need to be adjusted and explicitly verified for cement-based materials.
- Transport processes throughout the pore structure (i.e., from capillary to gel-pores) need to be addressed through multiscale models that account for the wide range of pore sizes (i.e., from the nano- to the micro-scale) and heterogeneous phase distribution among pore sizes.
- The verification of the models mentioned above requires tailored experiments that need to have a sufficient level of detail (both for input and output data) to describe the individual transport and reaction mechanisms.

Integration of RMT models into existing service-life design methodologies

This investigation has shown that RMT models can perform robust and time-efficient calculations to estimate durability-related parameters for the service life design of reinforced concrete structures.

However, implementation in existing service-life modeling frameworks requires further research in the following areas:

- Verification of model inputs utilizing existing test methods, for example, based on ponding (e.g., NTBuild 443 and AASHTO T259) or electromigration techniques (e.g., NT Build 492 or AASHTO T277) to calibrate key model input parameters (e.g., the tortuosity factor) that may be used as a reference design parameter
- The simplification of model input parameters (e.g., binder combination and phase assemblage pre-selection) based on a set of relevant reference case studies to facilitate the use of the RMT model approach by general designers in practical engineering applications. In this aspect, the combination of machine-learning techniques to RMT models shall be explored to simplify existing reaction models, as well as a mix-design optimization tool.
  The benchmarking of model predictions with existing performance-based models (e.g., fib 34), considering a reference structure or test-coupons. This aspect shall be oriented to identify relevant advantages and pitfalls of RMT models compared to traditional analytical transport models.

REFERENCES

[1] European Commitee for Standardization (CEN), Concrete. Specification, performance, production and conformity. EN 206, European Union, 2013.

[2] International Federation for Structural Concrete, Model Code for Service Life Design. MC-SLD:2006, Lausanne, Switzerland, 2006.

[3] Concrete Society, CS176 - Performance-Based Durability Design for Concrete, 2019.

[4] M. Bartholomew, C. Edvardsen, M. Ferreira, S. von Greve-Dierfeld, J. Gulikers, S. Helland, G. Markeset, P. McKenna, F. Papworth, B. Pielstick, A. Rahimi, fib Bulletin 76 - Benchmarking of deemed-to-satisfy provisions in standards, 2015.

[5] M. Šomodíková, A. Strauss, I. Zambon, fib models for modeling of chloride ion ingress and concrete carbonation: Levels of assessment of input parameters, Struct. Concr. 21 (2020). doi:10.1002/suco.201900401.

[6] J. Gulikers, Considerations on the reliability of service life predictions using a probabilistic approach, J. Phys. IV. 136 (2006) 233–241. doi:10.1051/jp4:2006136024.

[7] T. Luping, J. Gulikers, On the mathematics of time-dependent apparent chloride diffusion coefficient in concrete, Cem. Concr. Res. 37 (2007) 589–595. doi:10.1016/j.cemconres.2007.01.006.

[8] U. Angst, Chloride induced reinforcement corrosion in concrete Concept of critical chloride content-methods and, n.d.

[9] a Lindvall, DuraCrete-Probabilistic performance based durability design of concrete structures, in: 2nd Int. PhD. Symp. Civ. Eng., 1998: pp. 1–10.

[10] A. Attari, C. McNally, M.G. Richardson, A probabilistic assessment of the influence of age factor on the service life of concretes with limestone cement/GGBS binders, Constr. Build. Mater. 111 (2016) 488–494. doi:10.1016/j.conbuildmat.2016.02.113.

[11] M. Šomodíková, A. Strauss, I. Zambon, B. Teplý, Quantification of parameters for modeling of chloride ion ingress into concrete, Struct. Concr. 20 (2019) 519–536. doi:10.1002/suco.201800049.

[12] J. Marchand, E. Samson, Predicting the service-life of concrete structures--limitations of simplified models, Cem. Concr. Compos. 31 (2009) 515–521.

[13] J. Poonoosamy, C. Wanner, P. Alt Epping, J.F. Águila, J. Samper, L. Montenegro, M. Xie, D. Su, K.U. Mayer, U. Mäder, L.R. Van Loon, G. Kosakowski, Benchmarking of reactive transport codes for 2D simulations with mineral dissolution–precipitation reactions and feedback on transport parameters, Comput. Geosci. (2018) 1–22. doi:10.1007/s10596-018-9793-x.

[14] M.M. Jensen, B. Johannesson, M.R. Geiker, A Numerical Comparison of Ionic Multi-Species Diffusion with and without Sorption Hysteresis for Cement-Based Materials, Transp. Porous Media. 107 (2015) 27–47. doi:10.1007/s11242-014-0423-3.

[15] N.C.M. Marty, O. Bildstein, P. Blanc, F. Claret, B. Cochepin, E.C. Gaucher, D. Jacques, J.E. Lartigue, S. Liu, K.U. Mayer, J.C.L. Meeussen, I. Munier, I. Pointeau, D. Su, C.I. Steefel, Benchmarks for multicomponent reactive transport across a cement/clay interface, Comput. Geosci. 19 (2015) 635–653. doi:10.1007/s10596-014-9463-6.

[16] E. Samson, E. Grégoire, D. Leng, Optimizing the service life of concrete structures exposed to

chloride using modeling and field data, in: NACE - Int. Corros. Conf. Ser., NACE International, 2017: pp. 2222–2234.

[17] M. Alexander, H. Beushausen, Durability, service life prediction, and modelling for reinforced concrete structures – review and critique, Cem. Concr. Res. 122 (2019) 17–29. doi:10.1016/j.cemconres.2019.04.018.

[18] M.M. Jensen, A Coupled Transport and Chemical Model for Durability Pre-dictions of Cement Based Materials, 321 (2014) 208.

[19] A. Michel, V. Marcos-Meson, W. Kunther, M.R.R. Geiker, Microstructural changes and mass transport in cement-based materials: A modeling approach, Cem. Concr. Res. 139 (2021) 106285. doi:10.1016/j.cemconres.2020.106285.

[20] U. Angst, B. Elsener, C.K. Larsen, Ø. Vennesland, Critical chloride content in reinforced concrete — A review, Cem. Concr. Res. 39 (2009) 1122–1138. doi:10.1016/j.cemconres.2009.08.006.

[21] L. Bertolini, B. Elsener, P. Pedeferri, E. Redaelli, R.B. Polder, Corrosion of Steel in Concrete: Prevention, Diagnosis, Repair, Second, John Wiley & Sons, 2013.

[22] K. De Weerdt, G. Plusquellec, A. Belda Revert, M.R.R. Geiker, B. Lothenbach, Effect of carbonation on the pore solution of mortar, Cem. Concr. Res. 118 (2019) 38–56. doi:10.1016/j.cemconres.2019.02.004.

[23] K. De Weerdt, B. Lothenbach, M.R. Geiker, Comparing chloride ingress from seawater and NaCl solution in Portland cement mortar, Cem. Concr. Res. 115 (2019) 80–89. doi:10.1016/j.cemconres.2018.09.014.

[24] Z. Shi, M.R. Geiker, K. De Weerdt, T.A. Østnor, B. Lothenbach, F. Winnefeld, J. Skibsted, Role of calcium on chloride binding in hydrated Portland cement–metakaolin–limestone blends, Cem. Concr. Res. 95 (2017) 205–216. doi:10.1016/j.cemconres.2017.02.003.

[25] K. De Weerdt, M. Ben Haha, G. Le Saout, K.O. Kjellsen, H. Justnes, B. Lothenbach, Hydration mechanisms of ternary Portland cements containing limestone powder and fly ash, Cem. Concr. Res. 41 (2011) 279–291. doi:10.1016/j.cemconres.2010.11.014.

[26] Z. Shi, M.R. Geiker, B. Lothenbach, K. De Weerdt, S.F. Garzón, K. Enemark-Rasmussen, J. Skibsted, Friedel's salt profiles from thermogravimetric analysis and thermodynamic modelling of Portland cement-based mortars exposed to sodium chloride solution, Cem. Concr. Compos. 78 (2017) 73–83. doi:10.1016/j.cemconcomp.2017.01.002.

[27] Z. Shi, B. Lothenbach, M.R. Geiker, J. Kaufmann, A. Leemann, S. Ferreiro, J. Skibsted, Experimental studies and thermodynamic modeling of the carbonation of Portland cement, metakaolin and limestone mortars, Cem. Concr. Res. 88 (2016) 60–72. doi:10.1016/j.cemconres.2016.06.006.

[28] M. Geiker, T. Danner, A. Michel, A.B. Reverta, O. Linderothd, K. Hornbostel, 25 years field exposure of pre-cracked concrete beams; combined impact of spacers and cracks on reinforcement corrosion (unpublished), (2019) 1–35.

[29] E. Jones, M. Chierici, I. Skjelvan, M. Norli, K.Y. Børsheim, H.H. Lødemel, T. Kutti, K. Sørensen, A.L. King, K. Jackson, T. de Lange, Monitoring of ocean acidification in Norwegian seas in 2017, 2018.

[30] T. Danner, U. Hjorth Jakobsen, M.R. Geiker, U.H. Jakobsen, M.R. Geiker, Mineralogical Sequence of Self-Healing Products in Cracked Marine Concrete, Minerals. 9 (2019) 284. doi:10.3390/min9050284.

[31] T. Kanstad, S. Jacobsen, Green Concrete mix design: Robust Eco-friendly C100 concrete from

particle packing to bridge tower analysis in the «Ferry-free E39-project»., in: Konf. Nord. Vegforum, 2021.

[32] T. Kanstad, From 0 to C100 on 91 days – Eco-concrete for slipforming on E39, in: Teknologidagene, 2019.

[33] V. Marcos-Meson, Reactive Mass Transport model results - Chloride ingress in Norway (Dataset, Mendeley Data), (2021). doi:10.17632/jhzwn27rjn.1.

[34] D.L. Parkhurst, C.A.J. Appelo, Description of Input and Examples for PHREEQC Version 3—A Computer Program for Speciation, Batch-Reaction, One-Dimensional Transport, and Inverse Geochemical Calculations, US Geol. Surv. Tech. …. (2013).

[35] B. Lothenbach, D.A. Kulik, T. Matschei, M. Balonis, L. Baquerizo, B. Dilnesa, G.D. Miron, R.J. Myers, Cemdata18: A chemical thermodynamic database for hydrated Portland cements and alkali-activated materials, Cem. Concr. Res. 115 (2019) 472–506. doi:10.1016/j.cemconres.2018.04.018.

[36] M. Glissner, Service life prediction of concrete in cold climate , benchmarking of chloride ingress, NTNU - DTU, 2020.

[37] O. Zienkiewicz, The Finite Element Method: its Basis and Fundamentals, Elsevier, 2013. doi:10.1016/C2009-0-24909-9.

[38] G.A. Scheffler, R. Plagge, A whole range hygric material model: Modelling liquid and vapour transport properties in porous media, Int. J. Heat Mass Transf. 53 (2010) 286–296. doi:10.1016/j.ijheatmasstransfer.2009.09.030.

[39] A. Michel, V.M. Meson, H. Stang, M.R. Geiker, M. Lepech, Coupled mass transport, chemical, and mechanical modelling in cementitious materials: A dual-lattice approach, in: R. Caspeele, L. Taerwe, D.M. Frangopol (Eds.), Life Cycle Anal. Assess. Civ. Eng. Towar. an Integr. Vis. Proc. Sixth Int. Symp. Life-Cycle Civ. Eng. (IALCCE 2018), CRC Press, Ghent, Belgium, 2018: pp. 965–972.

[40] D.L. Parkhurst, C.A.J. Appelo, Description of Input and Examples for PHREEQC Inverse Geochemical Calculations Batch-Reaction, One-Dimensional Transport, and Version 3—A Computer Program for Speciation, Cso. (2005) 6-43A. doi:10.1016/0029-6554(94)90020-5.

[41] K. De Weerdt, H. Justnes, M.R. Geiker, Changes in the phase assemblage of concrete exposed to sea water, Cem. Concr. Compos. 47 (2014) 53–63. doi:10.1016/j.cemconcomp.2013.09.015.

[42] U.H. Jakobsen, K. De Weerdt, M.R. Geiker, Elemental zonation in marine concrete, Cem. Concr. Res. 85 (2016) 12–27. doi:10.1016/j.cemconres.2016.02.006.

[43] E. Hernandez-Bautista, D.P. Bentz, S. Sandoval-Torres, P.F.J. De Cano-Barrita, Numerical simulation of heat and mass transport during hydration of Portland cement mortar in semi-adiabatic and steam curing conditions, Cem. Concr. Compos. 69 (2016) 38–48. doi:10.1016/j.cemconcomp.2015.10.014.

[44] B. Lothenbach, K. Scrivener, R.D. Hooton, Supplementary cementitious materials, Cem. Concr. Res. 41 (2011) 1244–1256. doi:10.1016/j.cemconres.2010.12.001.

[45] P.T. Bui, Y. Ogawa, K. Kawai, Long-term pozzolanic reaction of fly ash in hardened cement-based paste internally activated by natural injection of saturated Ca(OH)2 solution, Mater. Struct. Constr. 51 (2018) 1–14. doi:10.1617/s11527-018-1274-0.

[46] F. Han, J. Liu, P. Yan, Comparative study of reaction degree of mineral admixture by selective dissolution and image analysis, Constr. Build. Mater. 114 (2016) 946–955. doi:10.1016/j.conbuildmat.2016.03.221.

[47] W. Liao, X. Sun, A. Kumar, H. Sun, H. Ma, Hydration of Binary Portland Cement Blends Containing Silica Fume: A Decoupling Method to Estimate Degrees of Hydration and Pozzolanic Reaction, Front. Mater. 6 (2019) 78. doi:10.3389/fmats.2019.00078.

[48] K. De Weerdt, K.O. Kjellsen, E. Sellevold, H. Justnes, Synergy between fly ash and limestone powder in ternary cements, Cem. Concr. Compos. 33 (2011) 30–38. doi:10.1016/j.cemconcomp.2010.09.006.

[49] Mathworks, Statistics and Machine Learning Toolbox, (2020).

[50] L. Breiman, Random Forests, 2001.

[51] L. Breiman, J.H. Friedman, R.A. Olshen, C.J. Stone, Classification and regression trees, CRC Press, 2017. doi:10.1201/9781315139470.

[52] S. Fjendbo, H.E. Sørensen, K. De Weerdt, U.H. Jakobsen, M.R. Geiker, Correlation of chloride profiles in marine exposed concrete with microstructural and moisture changes (unpublished), Cem. Concr. Compos. (n.d.).

[53] S. Sharmilan, H. Stang, A. Michel, A multi-species reactive transport model based on ion-solid phase interaction for saturated cement-based materials (unpublished), Cem. Concr. Res. (2022).

[54] Q. Zeng, K. Li, T. Fen-Chong, P. Dangla, Pore structure characterization of cement pastes blended with high-volume fly-ash, Cem. Concr. Res. 42 (2012) 194–204. doi:10.1016/j.cemconres.2011.09.012.

[55] D.K. Panesar, R. Zhang, Performance comparison of cement replacing materials in concrete: Limestone fillers and supplementary cementing materials – A review, Constr. Build. Mater. 251 (2020) 118866. doi:10.1016/j.conbuildmat.2020.118866.

[56] A. Michel, Reinforcement Corrosion: Numerical Simulation and Service Life Prediction, 2012.

APPENDIXES

Appendix A: Pre-study

Appendix B: Input data

Appendix C: Comparison to mix-design from E39

Appendix A: Pre-study

This appendix contains the reaction simulations part of the pre-study to verify the chemical reaction model used on the RMT simulations.

A1. Reference case 1: Laboratory exposure

Phase assembly for hydration of white Portland cement at fixed w/b ratio. Main binder: White Portland cement clinker (wPC).

Table A1 Parameters for the calculation

Parameter	Units	Value
w/b ratio	[-]	0.50
Alpha	[-]	0 – 1
White PC (wPC)	%-wt	100

Observations:

1) Similar phase assembly to PC
2) Limited Fe in solution

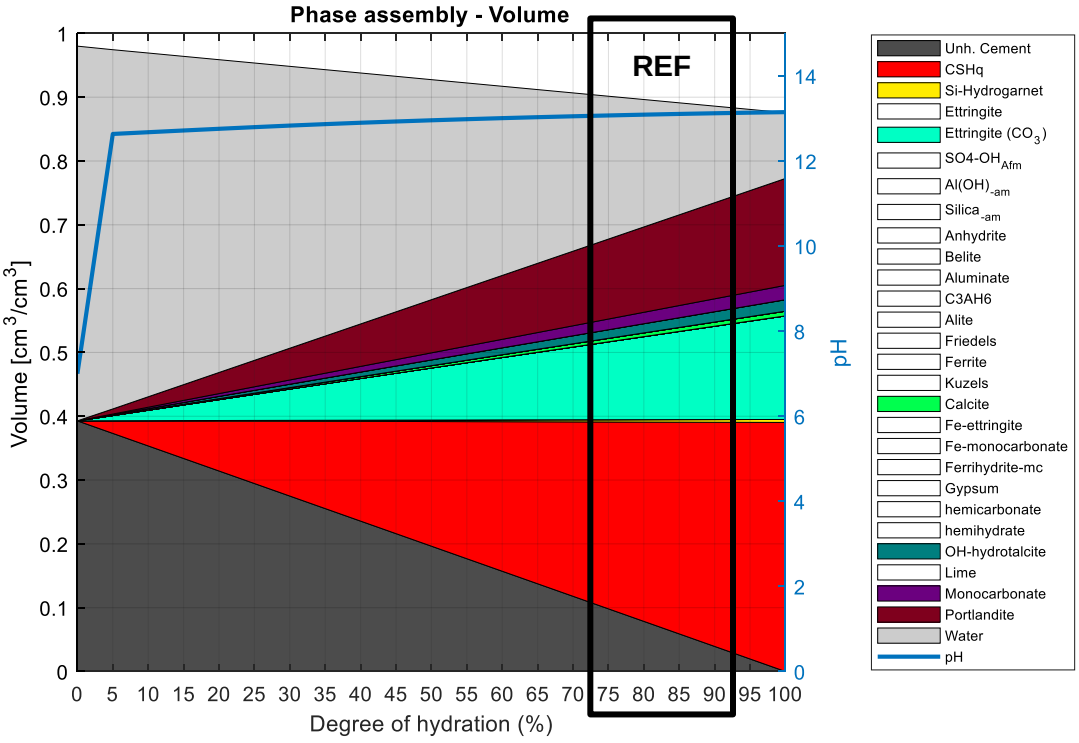

Fig. A1 Phase assembly, white Portland cement vs degree of hydration.

A2. Reference case 2: Field exposure

A2.1. Blended PC with FA and SF: Beam B

Phase assembly for hydration of blended Portland cement (with SF), for case B.

Table A2 Parameters for the calculation

Parameter	Units	Value
w/b ratio	[-]	0.415
Alpha	[-]	0 – 1
PC	%-wt	96.2
FA	%-wt	0.00
SF	%-wt	3.8

Observations:

1) Free Portlandite available
2) Unknown degree of hydration at time of exposure in ref. (assumed 80%)
3) Unknown entrained air content at time of exposure. Assumed 5%-vol.
4) CO2 of blended mix reasonable. Some calcite present.

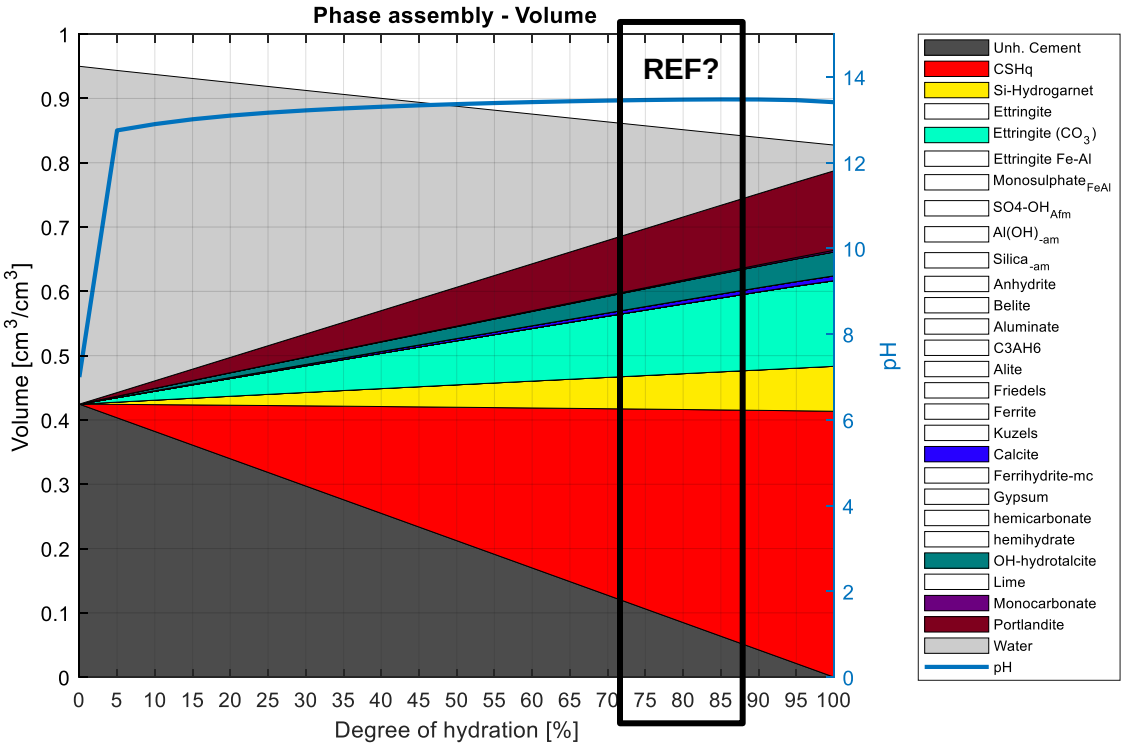

Fig. A2 Phase assembly, Portland cement + SF vs degree of hydration.

A2.2. Blended PC with FA and SF: Beam E

Phase assembly for hydration of blended Portland cement (with FA and SF), for case E.

Table A3 Parameters for the calculation

Parameter	Units	Value
w/b ratio	[-]	0.415
Alpha	[-]	0 – 1
PC	%-wt	80.1
FA	%-wt	16.0
SF	%-wt	3.9

Observations:

1) Consumed all Portlandite
2) Unknown degree of hydration at time of exposure in ref. (assumed 75%)
3) Unknown entrained air content at time of exposure. Assumed 5%-vol.
4) CO2 of blended mix increase, so that SO4-(OH)afm is in phase assembly as Ettringite

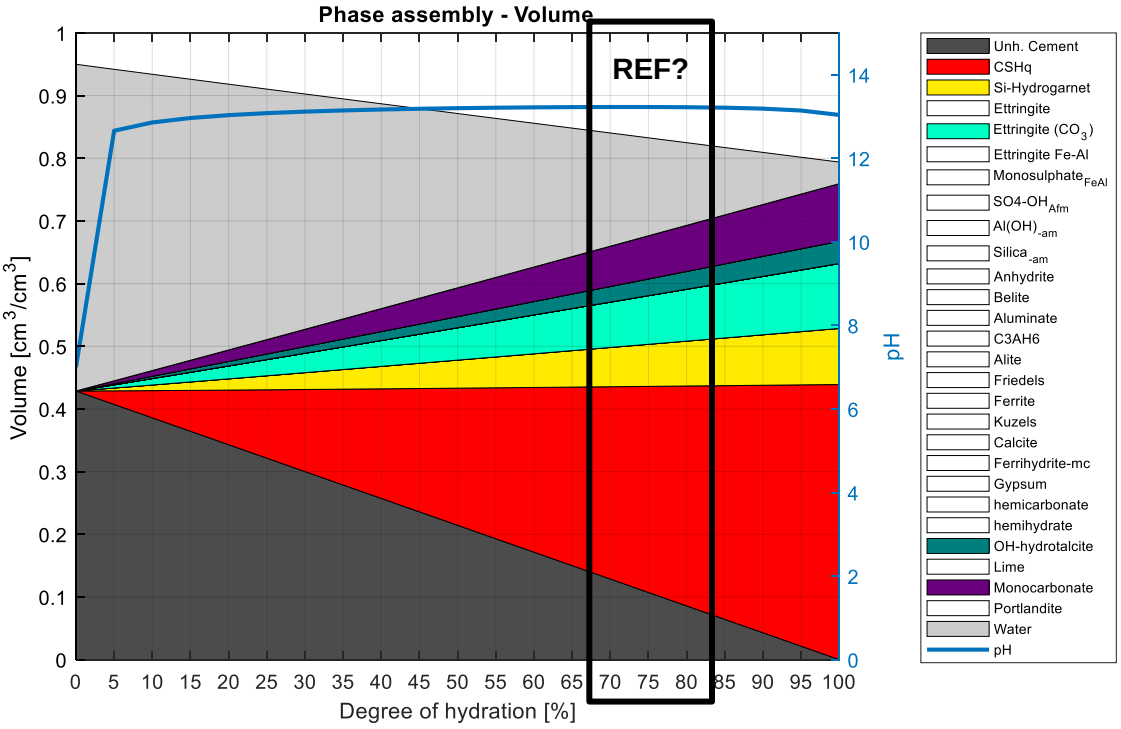

Fig. A3 Phase assembly, Portland cement + FA + SF vs degree of hydration.

A2.3. Blended PC with FA and SF: Beam F

Phase assembly for hydration of blended Portland cement (with SF), for case F.

Table A4 Parameters for the calculation

Parameter	Units	Value
w/b ratio	[-]	0.443
Alpha	[-]	0 – 1
PC	%-wt	89.3
FA	%-wt	0.0
SF	%-wt	10.7

Observations:

1) Free Portlandite available (close to limit)
2) Larger volume of C-S-H compared to case B. Higher pore volume (due to higher w/b)
3) Unknown degree of hydration at time of exposure in ref. (assumed 80%)
4) Unknown entrained air content at time of exposure. Assumed 5%-vol.
5) CO2 of blended mix is reasonable. Some calcite present.

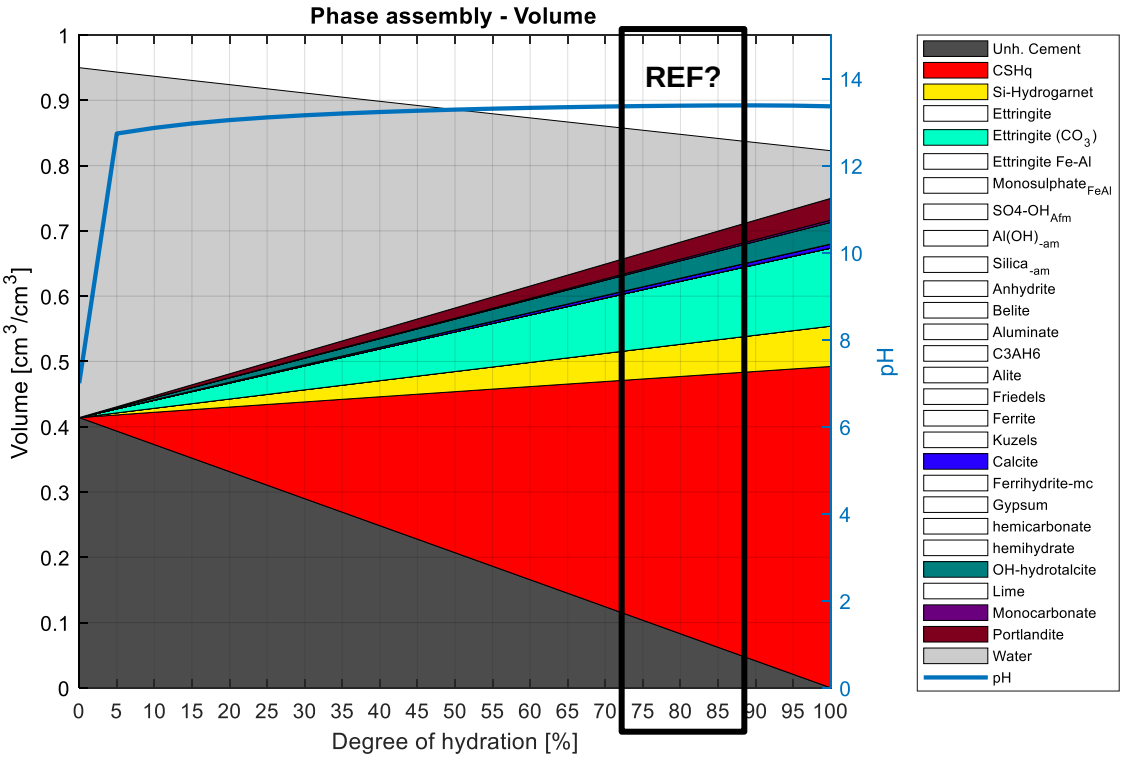

Fig. A4 Phase assembly, Portland cement + FA + SF vs degree of hydration.

A3. Replacement of PC

A3.1. Case 1: Replacement of PC with FA

Phase assembly for replacement of Portland cement clinker with Fly Ash.

1) Main binder: Portland cement clinker (PC)
2) Replacement: Fly ash (FA) 0 – 40 %-wt.

Table A5 Input parameters for Case 1

Parameter	Units	Value
w/b ratio	[-]	0.35
Alpha	[-]	0.75
Fly Ash (FA)	%-wt	0 – 40

Observations:

1) Drop of pH after 15-16% replacement (consumption of CH)
2) Formation of various Ettringite phases (aft afm) → those will be combined in final plots as Ettringite
3) Reduction in volume after approx. 6% replacement.
4) Formation of Al(OH) after approx. 24% replacement. Excess of alumina.
   a) Consider including Zeolite in phases to take over the Al(OH).

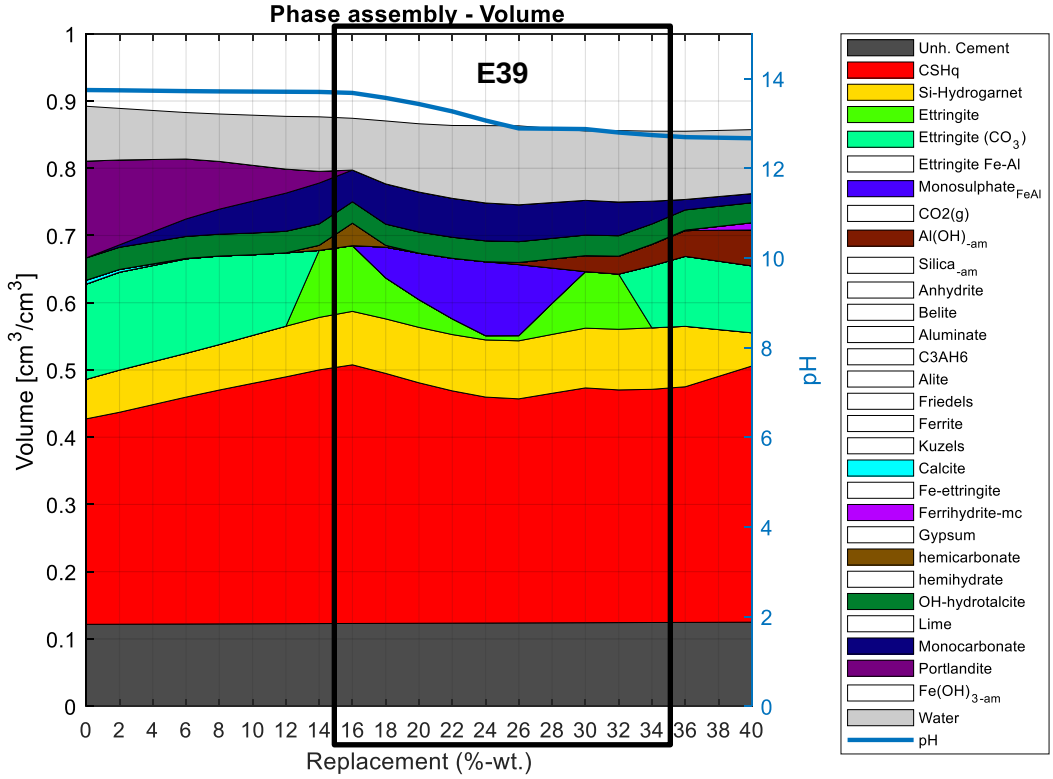

Fig. A5 Case 1: Phase assembly, Portland cement with replacement with FA

A4. Case 2: Replacement of PC with FA and SF

A4.1. Case 2a: Replacement of PC with variable content of FA and fixed SF

Phase assembly for replacement of Portland cement (PC) clinker with Fly Ash (FA).

1) Main binder: Portland cement clinker (PC)
2) Replacement: Fly ash (FA) 0 – 40 %-wt.
3) Replacement of SF at 5%-wt (fixed).

Table A6 Input parameters for Case 2a

Parameter	Units	Value
w/b ratio	[-]	0.35
Alpha	[-]	0.75
Fly Ash (FA)	%-wt	0 – 40
Silica Fume (SF)	%-wt	5

Observations:

1) Similar behaviour to PC+FA
2) Earlier consumption of Portlandite and drop of pH (approx. at 15% replacement of PC)
3) Reduction in volume after approx. 6% replacement.
4) Formation of Al(OH) after approx. 24% replacement. Excess of alumina.
5) Larger volume of C-S-H compared to PC+FA

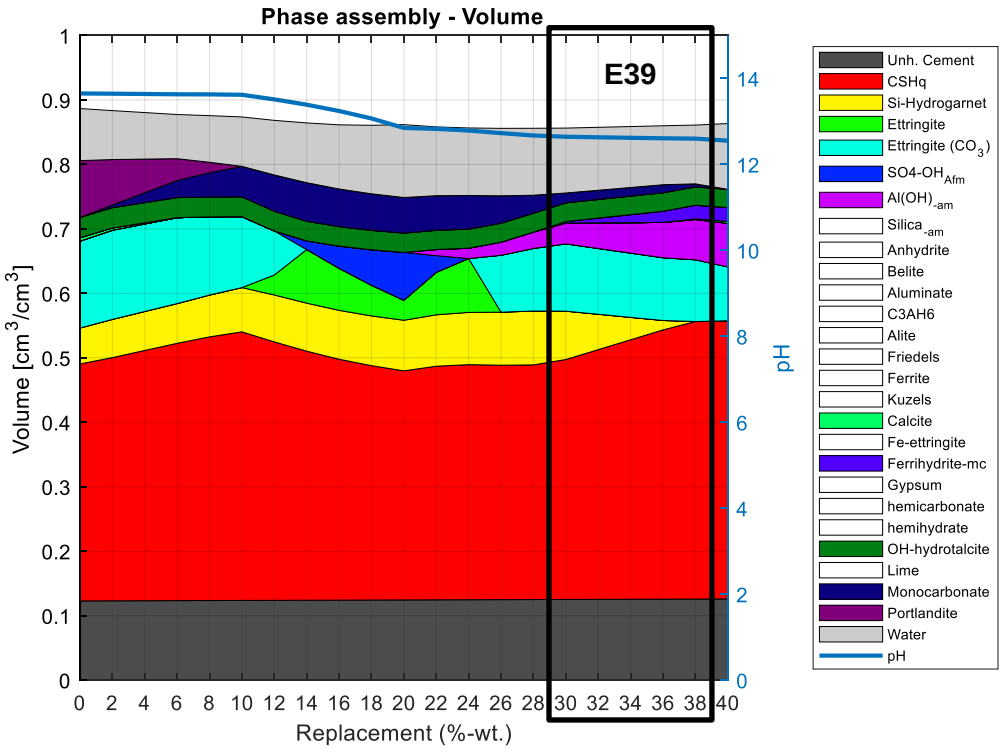

Fig. A6 Case 2a: Phase assembly, Portland cement with variable replacement of FA (0-40 %-wt). Considering 5%-wt. of SF.

A4.2. Case 2b: Replacement of PC with fixed content of FA and variable SF

Phase assembly for replacement of Portland cement clinker with Fly Ash (FA) and Silica Fume (SF).

1) Main binder: Portland cement clinker (PC)
2) Replacement: Fly ash (FA) 15 %-wt.
3) Replacement of SF in range 0 – 20 %-wt.

Table A7 Input parameters for Case 2b

Parameter	Units	Value
w/b ratio	[-]	0.35
Alpha	[-]	0.75
Fly Ash (FA)	%-wt	15
Silica Fume (SF)	%-wt	0 – 20

Observations:

1) Similar behaviour to PC+FA
2) Less aluminates and higher C-S-H volume
3) Volume increase of C-S-H

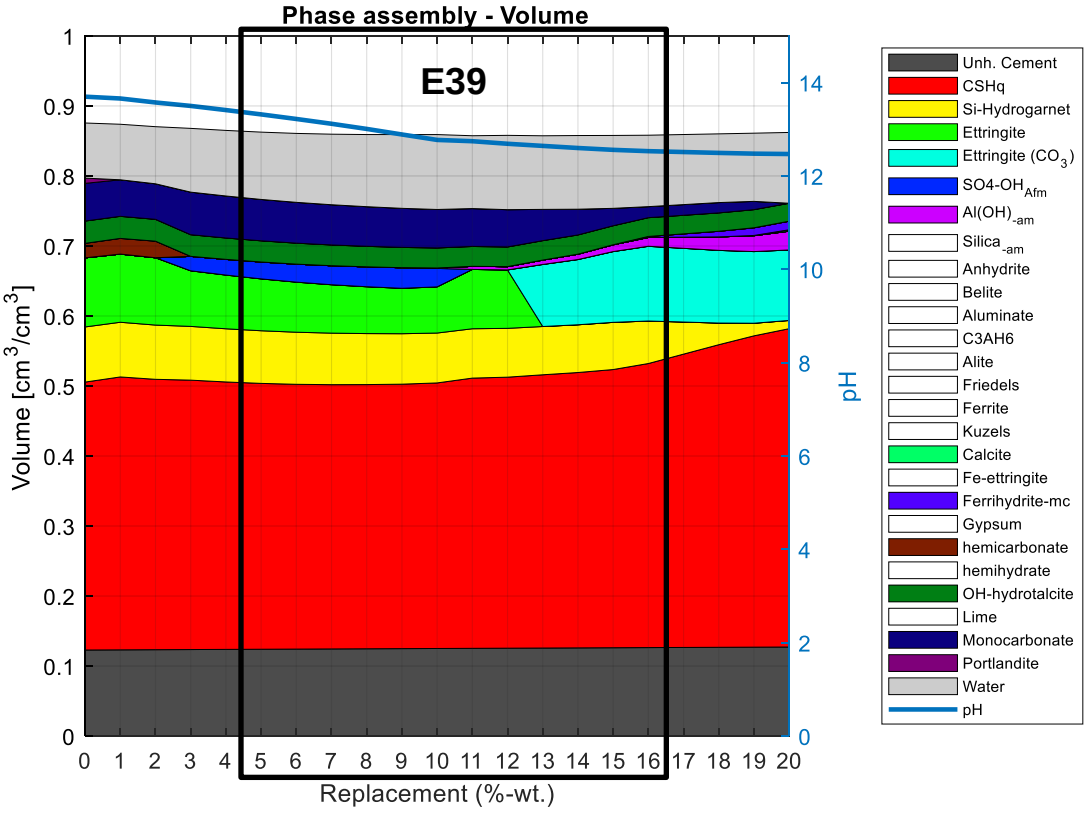

Fig. A7 Case 2b: Phase assembly, Portland cement with replacement of SF (0-20 %-wt). Considering 15%-wt. of FA.

A4.3. Case 3: Replacement of PC with MK

Phase assembly for replacement of Portland cement clinker with Metakaolin (MK).

1) Main binder: Portland cement clinker (PC)
2) Replacement: Metakaolin (MK) 0 – 40 %-wt.

Table A8 Input parameters for Case 3

Parameter	Units	Value
w/b ratio	[-]	0.35
Alpha	[-]	0.75
Metakaolin (MK)	%-wt	0 – 40

Observations:

1) Decrease of pH with increasing replacement:
   a) Minor after consumption of Portlandite (at 15% replacement)
   b) Substantial after consumption of Si-Hydr. (at 30% replacement)
2) Overall volume increase. Substantial due to formation of Strängelite (as in [26])

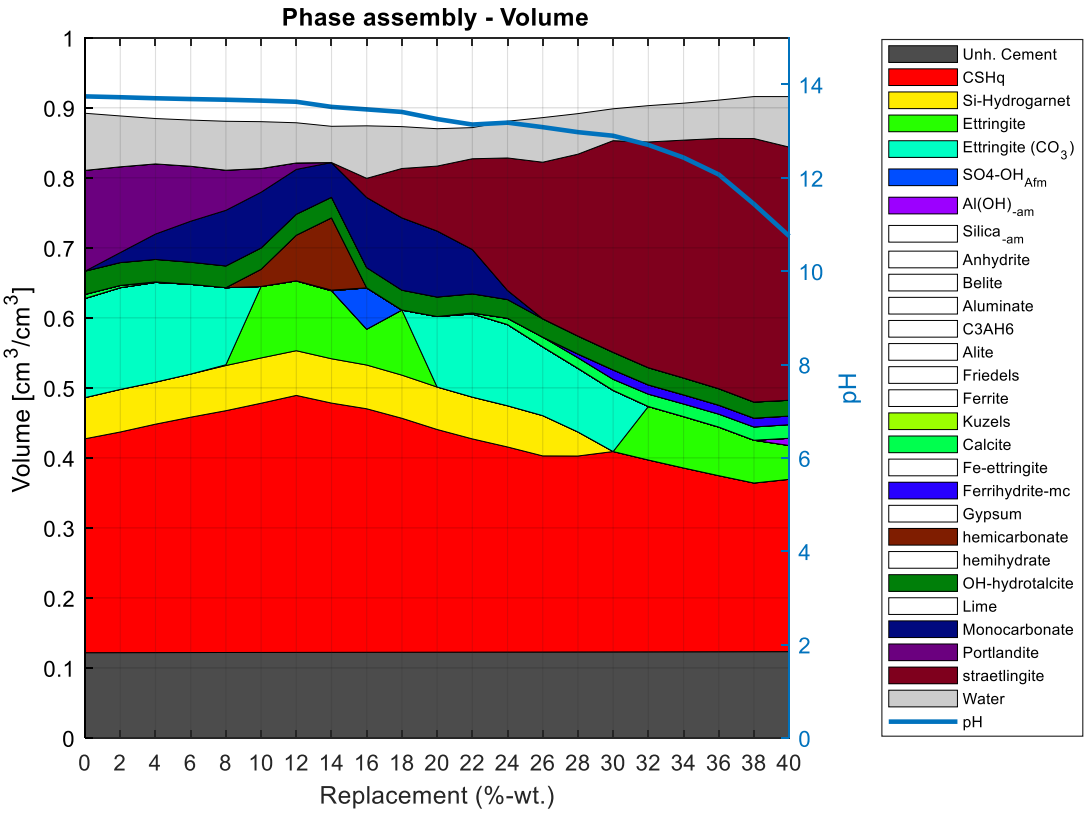

Fig. A8 Phase assembly, Portland cement with replacement of MK (0-40 %-wt).

A5. Chloride binding

A5.1. Case 1: Chloride binding in laboratory exposure

Phase assembly for replacement of Portland cement clinker (after [26]).

1) Main binder: White Portland cement clinker (wPC)
2) Incremental addition of NaCl in water (i.e. as if in mixing water).

Table A9 Parameters for the calculation

Parameter	Units	Value
Alpha	%	85
w/b ratio	[-]	0.50
Binder		wPC
NaCl	mmol/l	0-200
CaCl2	mmol/l	0-200

a)

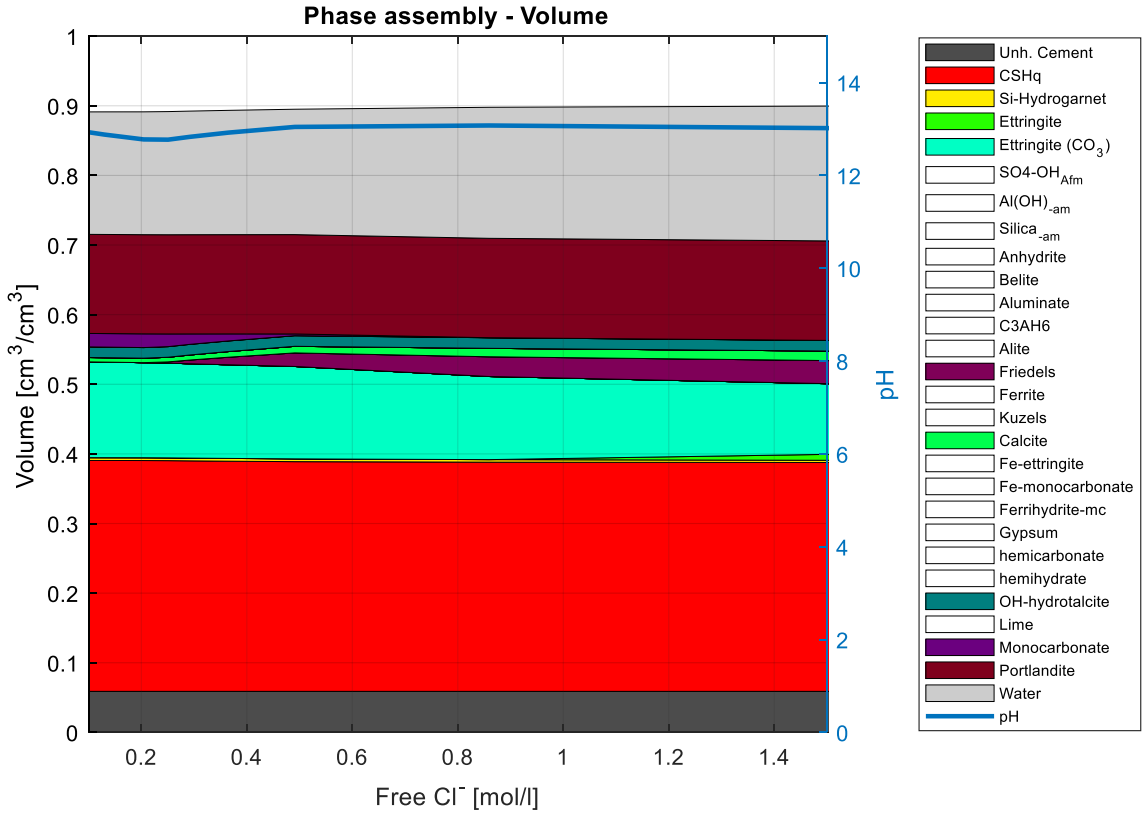

b)

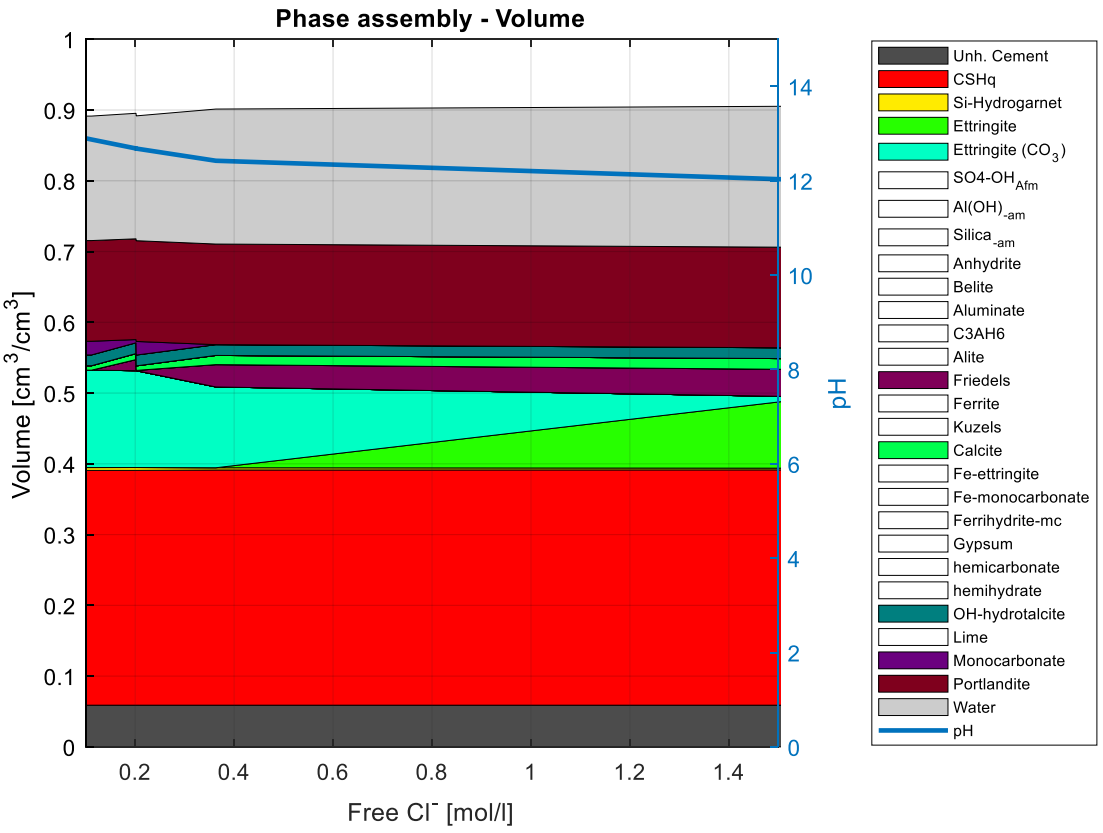

Fig. A9 Phase assembly, white Portland cement (α=0.85) with: a) increasing NaCl, b) increasing CaCl2.

A5.2. Case 2: Chloride binding in field exposure: case E

Phase assembly considering formation of:

1) Main binder: Portland cement clinker (PC)
2) Incremental addition of NaCl in solution (e.g. as in mixing water).

Table A10 Parameters for the calculation

Parameter	Units	Value
Alpha	%	85
w/b ratio	[-]	0.415
Binder		PC+FA+SF
Cl-	mmol/l	100-1500

Observations:

1) Friedels salt (FS) forming at approx. 400mmol/l
2) Moderate variation in pH.
3) FS substituting Monocarbonate

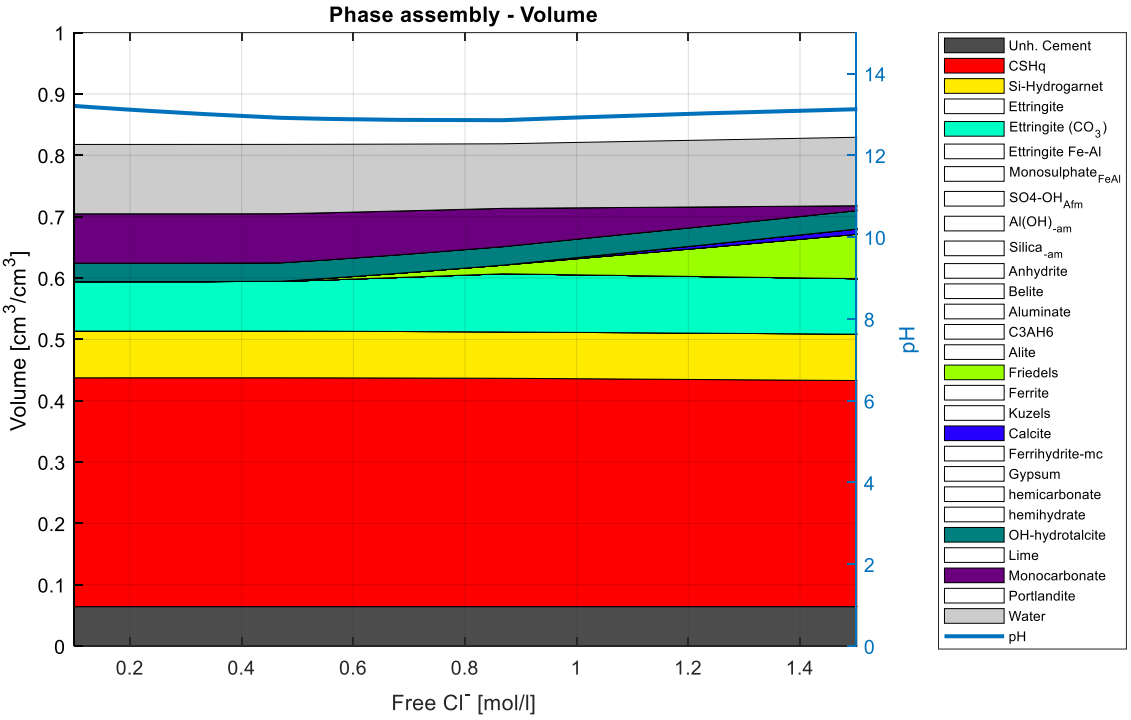

Fig. A10 Phase assembly, Blended Portland cement (PC+FA+SF) (α=0.85) with increasing NaCl in solution.

A5.3. Case 2: Chloride binding in field exposure: case F

Phase assembly considering formation of:

1) Main binder: Portland cement clinker (PC)
2) Incremental addition of NaCl in solution (e.g. as in mixing water).

Table A11 Parameters for the calculation

Parameter	Units	Value
Alpha	%	85
w/b ratio	[-]	0.443
Binder		PC+ SF
Cl-	mmol/l	100-1500

Observations:

1) Friedels salt forming at approx. 500mmol/l
2) Moderate drop in pH at formation of Friedels salt (FS)
3) FS substituting Ettringite

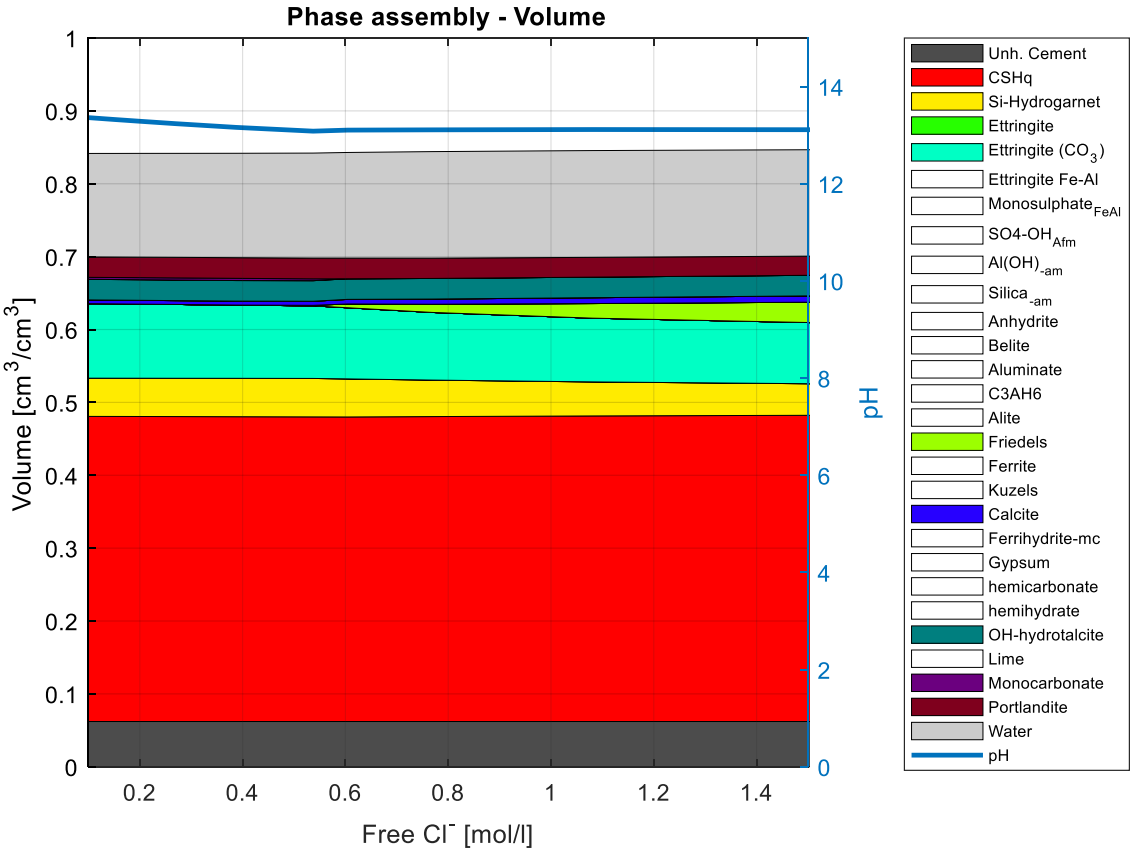

Fig. A11 Phase assembly, Blended Portland cement (PC+FA+SF) (α=0.85) with increasing NaCl in solution.

Appendix B: Model input data

The input parameters used in the model are summarized in the table below. The input parameters varied within the study (i.e. binder coxide composition and degree of hydration) are shown in the main report.

ID	VARIABLE	VALUE	UNITS	NOTES
Spatial parameters				
1	Total length	1	m	Total length simulated in the Sys (1D)
2	Area of interest	0.4	m	Reduces resolution outside interest area
3	Elements	50	-	Total number of elements
4	Growth factor	1.2	-	Growth factor "power-law" for spatial elements
5	Element area	1	m2	Cross-sectional area setup 1D Sys
Time parameters				
6	Total time	1752000	h	Total calculation time
7	Acceleration factor	1	-	Acceleration factor for transport calculation
8	Step size	720	h	Lenght of time step
9	Chemical interval	720	h	Chemical equilibrium interval
Hydration law				
10	Shape factor	30	-	Maturity parameter, shape factor
11	Reaction rate	0.35	-	Maturity parameter, reaction rate
12	Activation Energy	25000	J/mol	Activation Energy (calibrated)
13	Temperature hydration	278.15	K	Temperature (hydration law)
14	Reference temp.	293.15	K	Reference temperature M20
15	Curing time	28	days	Maturity M20 before exposure
16	Referenc maturity	28	days	Reference maturity M20
Mix-design				
17	Water-binder ratio	0.35	-	Water-binder ratio
18	Aggregate ratio	0.664	m3/m3	Tot. aggregate volume ratio
19	Agrregate density	2.65	g/cm3	Inert phase density
20	Entrained air	0.05	m3/m3	Entrained porosity
21	Ref. volume	1	m3/m3	Reference volume of solids
Pore structure				
22	Pore area	1	m2/m3	Total pore area
23	Reaction depth	0	m	Reaction depth at pore surface
24	Pore volume-area ratio	4.61E+06	m2/m3	Pore volume-area ratio (derived from PSD)
25	Pore radii (mean)	[1e-2, 1e0, 1e2]	um	Pore radius range [um] [gel,cap,macro] (mean)
26	Pore radii (sd)	[0.55, 0.85, 0.75]	-	Pore radius spread [gel,cap,macro] (COV)
27	Pore Change	[0.7, 0.25, 0.05]	-	Distribution of pore volume change [gel,cap,macro]
28	Ser-par connectivity	1.4	-	Serial-parallel conectivity
29	Global connectivity	2.9	-	Global liquid connectivity

30	Vapour diffusion	9	-	Dry vapour diffusion resistance
31	Moisture conductivity	1.00E-05	s	Effective conductivity at saturation
32	Contact angle	[15, 65]	deg	Contact angle (adsorption - desorption)
33	Surface tension	7.28E-02	N/m	Surface tension of water
Boundary				
34	Variable boundary	FALSE	T/F	Use variable boundary conditions
35	No-flux boundary	FALSE	T/F	Limit outflux trough boundary
36	Pressure (boundary 1)	NaN	Pa	The relative humidity at boundary. (NaN omit)
37	Pressure (boundary 2)	NaN	Pa	
38	Current (boundary 1)	0	C	The imposed potential at the boundary. 0 = equilibrium of charge. NaN if ommitted
39	Current (boundary 2)	NaN	C	
Other				
40	Initial moisture flux	0	(0/1)	Initial moisture flux direction [Adsorption=0, Desorption=1]
41	Saturation	0.9	m3/m3	Force a specific saturation degree on the whole domain. If NaN, saturation is determined from the chemical equilibrium calculation. If Moisture transport, saturation is only enforced for the curing step.
42	Stream Upwinding coefficient	2	-	Advective transport upwinding (Stream Upwinding coefficient). Values [0-(1)-(~=10)] (1 = optimum) (>1 = over-diffusive)
43	Initial tortuosity factor	0.01	-	Tortuosity function. Reference tortuosity at t=0
44	Tortuosity shape	1		Tortuosity function. Shape factor (e.g 0-5, 0 = no tort.changes)
45	Tortuosity limit	0.0001		Tortuosity function. Tortuosity limit (lower asymptote) (avoid 0!)
Chloride binding				
46	Physical Binding	TRUE	T/F	Physical binding in CHS gel (based on binding isotherm)
47	Binding mode	1	1/2	Physical binding mode (after or before equilibrium)
48	Isotherm parameters	[2.3,2.3, 0.001,1]	-	Parameters for "modified" Lagumir isotherm [Ka, Kb, Pa]

The ions considered in the simulation, as per CEMDATA 18 [35].

ID	**ION**		**ID**	**ION**		**ID**	**ION**
1	OH-		26	Fe+2		53	Na+
2	H+		27	FeCO3		54	Na(SO4)-
3	O2		28	Fe(SO4)		55	NaCO3-
5	AlO2-		29	Fe+3		56	NaHCO3
6	AlO2H		30	Fe(SO4)+		57	SiO3-2
7	AlSiO5-3		31	FeHCO3+		58	HSiO3-
8	AlO+		32	FeHSiO3+2		62	S2O3-2
9	Al(OH)+2		33	Fe(SO4)2-		63	SO3-2
10	Al+3		34	FeHSO4+		64	SO4-2

11	Al(SO4)+		38	FeCl+		65	HSO4-
12	Al(SO4)2-		39	FeCl+2		67	HSO3-
13	AlHSiO3+2		40	FeCl2+		68	S-2
14	Ca(OH)+		41	FeCl3		69	CO2
15	Ca+2		42	K+		71	CO3-2
16	CaSO4		43	KOH		72	HCO3-
17	CaCO3		44	KSO4-		73	Cl-
18	CaSiO3		45	Mg(OH)+		74	ClO4-
19	Ca(HCO3)+		46	Mg+2			
20	Ca(HSiO3)+		47	Mg(SO4)			
21	FeO2-		48	Mg(CO3)			
22	FeO2H		49	MgSiO3			
23	FeO+		50	Mg(HCO3)+			
24	Fe(OH)+2		51	Mg(HSiO3)+			
25	FeOH+		52	NaOH			

The equilibrium phases and solid solutions considered in the simulations, as per CEMDATA 18 [35].

ID	**Equilibrium phase**
10	'AlOHam'
12	'Amor-Sl'
15	'Brc'
29	Friedels'
34	Kuzels'
40	Cal'
75	'FeOOHmic'
77	'Gp'
82	'hemicarbonate'
84	'hemihydrate'
85	'hydrotalcite'
94	'Lim'
107	'monocarbonate'
120	'Portlandite'
132	'thaumasite'
	Solid Solution phase
1	'CSHQ'
2	'C3(AF)S0.84H'
3	ettringite'
4	SO4_CO3_AFt'
5	ettringite-FeAl'
6	monosulph-FeAl'

Appendix C: Comparison with reference study

This appendix contains a comparison of the range simulated in this study and the experimental data produced in the reference study in [31,32].

Experimental - E39 Sulafjorden (utvalgt for ytterligere forsøk 3, 4, 12, 14)												Simulations		
Blanding		1	2	3	4	5	6	11	12	13	14	Min	Max	Default
Kode (v/b matriks)		0.35 315	0.35 325	0.35 335	0.30 335	0.35 335 FA	0.30 335 FA	0.35 335 8Si	0.35 335 16Si	0.30 335 8Si	030 335 16Si			
Paste vol %		30	31	32	32	31	31	30	30	30	30	25	25	25
w/b		0.36	0.36	0.36	0.31	0.34	0.29	0.36	0.39	0.31	0.33	0.35	0.35	0.35
v/c+2s+0.7tilsFA (maks 35 % FA tot)		0,35	0,35	0,35	0,30	0,39	0,33	0,375	0,38	0,32	0,32			
v/c+2s+0.7tilsFA (total FA)						0,35	0,30	0,35	0,35	0,30	0,30			
Klinker	Kg/m3	355	367	382	410	287	307	267	226	287	243			
FA totalt		63	65	67	72	159	169	134	123	145	132			
Sement		418	432	449	482	338	361	314	266	338	286			
SF		13	13	14	15	14	15	35	66	38	72			
FA tilsatt						108	115	87	83	94	89			
Binder		431	445	463	497	460	491	436	415	470	447			
FA % av bind.		14.6	14.6	14.5	14.5	34.6	34.4	30.7	29.6	30.9	29.5	0	30	15
SF % av bind.		3.0	2.9	3.0	3.0	3.0	3.1	8.0	15.9	8.1	16.1	0	10	5
Vann		155	161	167	154	155	141	156	160	144	148			

This study comprises a feasibility study of reactive mass transport modelling to support the service life design of reinforced concrete structures exposed to chlorides.

The study was undertaken as part of the collaboration project “Fergefri E39, forskning knyttet til Gjennomføring, utførelse, analyse og dimensjonering av store og avanserte betongkonstruksjoner i utsatt miljø”, between Statens vegvesen and NTNU.

The work has been carried out by researcher/postdoc Victor Marcos Meson (DTU) in collaboration with Professor Mette Geiker (NTNU) and Professor Alexander Michel (DTU).